AGU PUBLICATIONS

Geochemistry, Geophysics, Geosystems

RESEARCH ARTICLE
10.1002/2015GC005956

Reactive transport in a partially molten system with binary solid solution

Jacob S. Jordan[1] and Marc A. Hesse[1,2]

[1]Department of Geological Sciences, University of Texas, Austin, Texas, USA, [2]Institute for Computational Engineering and Sciences, University of Texas, Austin, Texas, USA

Key Points:
- Framework for analysis of 1-D reactive melt transport with major element phase behavior
- Coupling of energy and mass during melting-freezing and dissolution-precipitation
- Prediction of porosity profiles identifies unstable and self-limiting reaction fronts

Correspondence to:
M. A. Hesse,
mhesse@jsg.utexas.edu

Citation:
Jordan, J. S., and M. A. Hesse (2015), Reactive transport in a partially molten system with binary solid solution, *Geochem. Geophys. Geosyst.*, *16*, 4153–4177, doi:10.1002/2015GC005956.

Received 10 JUN 2015
Accepted 16 OCT 2015
Accepted article online 23 OCT 2015
Published online 19 DEC 2015

Abstract Melt extraction from the Earth's mantle through high-porosity channels is required to explain the composition of the oceanic crust. Feedbacks from reactive melt transport are thought to localize melt into a network of high-porosity channels. Recent studies invoke lithological heterogeneities in the Earth's mantle to seed the localization of partial melts. Therefore, it is necessary to understand the reaction fronts that form as melt flows across the lithological interface between the heterogeneity and the ambient mantle. Here we present a chromatographic analysis of reactive melt transport across lithological boundaries, using the theory of hyperbolic conservation laws. This is an extension of linear trace element chromatography to the coupling of major elements and energy transport. Our analysis allows the prediction of the nonlinear feedbacks that arise in reactive melt transport due to changes in porosity. This study considers the special case of a partially molten porous medium with binary solid solution. As melt traverses a lithological contact, binary solid solution leads to the formation of a reacted zone between an advancing reaction front and the initial contact. The analysis also shows that the behavior of a fertile heterogeneity depends on its absolute concentration, in addition to compositional differences between itself and the refractory background. We present a regime diagram that predicts if melt emanating from a fertile heterogeneity localizes into high-porosity channels or develops a zero porosity shell. The theoretical framework presented here provides a useful tool for understanding nonlinear feedbacks in reactive melt transport, because it can be extended to more complex and realistic phase behaviors.

1. Introduction

Geological and petrological observations require that melt extraction below mid-ocean ridges is localized into high-porosity channels [*Kelemen et al.*, 1995, 1997]. The upper portions of these channels are thought to consist of dunite which allows melt extraction from depth without reequilibration [*Liang et al.*, 2010]. *Aharonov et al.* [1995] recognized that increasing orthopyroxene solubility with decreasing depth could provide a positive feedback mechanism to localize melt flow. Initial simulations of reactive melt transport in a compacting matrix show the spontaneous localization of melt into channels [*Spiegelman et al.*, 2001]. It is now generally accepted that reactive feedback mechanisms cause the channelization associated with dunite formation, although other purely mechanical mechanisms may also lead to melt localization [*Stevenson*, 1989; *Katz et al.*, 2006; *Keller et al.*, 2013].

Channel formation was not observed in subsequent studies which improved the model description by accounting for mantle upwelling, variable bulk viscosity, and melting induced either by the dissolution of orthopyroxene or the coupling of mass and energy transfer through phase behavior. For the orthopyroxene dissolution models, the growth rate of channels decreases with increasing upwelling and is dramatically lower in models where bulk viscosity decreases with increasing porosity [*Hesse et al.*, 2011]. For typical conditions beneath mid-ocean ridges, these models give rise to compaction-dissolution waves rather than high-porosity channels [*Liang et al.*, 2011]. For models that couple mass and energy transfer, the melting rate increases with upwelling and increasing thermal diffusivity, but it is inversely proportional to the latent heat of fusion [*Hewitt*, 2010; *Katz and Rudge*, 2011; *Weatherley and Katz*, 2012]. For preferred mantle properties, these models show that the melt flux from a homogeneous mantle is insufficient to trigger spontaneous channelization [*Hewitt*, 2010; *Weatherley and Katz*, 2012]. However, in both types of models, fusible heterogeneities can supply a melt flux sufficient for channelization [*Liang et al.*, 2010; *Weatherley and Katz*, 2012]. This highlights the role of lithological heterogeneities in the Earth's mantle as potential seeds for the nucleation of high-porosity channels.

During partial melting, fusible lithological heterogeneities with a lower solidus produce local regions of high porosity. Reaction fronts develop as melt advects from heterogeneities across a lithological boundary into the ambient mantle. An upstream increase in porosity across a reaction front can cause a reaction infiltration instability that is characterized by scalloping of the reaction front and the eventual localization of melt flow into high-porosity fingers [*Chadam et al*., 1986; *Hinch and Bhatt*, 1990; *Szymczak and Ladd*, 2013; *Pec et al*., 2015]. Therefore, the key to understand if a heterogeneity will seed high-porosity channels is the change in porosity across the reaction front. Although the reaction infiltration instability is intrinsically a multidimensional phenomenon, changes in porosity across a reaction front can be predicted using one-dimensional analysis.

The reactive transport due to the advection of melt across a lithological interface can be represented as a one-dimensional problem with an initial discontinuity separating two regions, also known as a Riemann problem. In the limit of local thermodynamic equilibrium, negligible hydrodynamic dispersion, and a rigid porous medium, the equations governing reactive melt transport reduce to a system of quasi-linear hyperbolic equations. In this limit, the theory of hyperbolic equations allows a full analysis of Riemann problems [*Lax*, 1973; *LeVeque*, 1991]. In the context of reactive transport in porous media, this approach is commonly referred to as the theory of chromatography [*DeVault*, 1943; *Glueckauf*, 1945; *Rhee et al*., 1989; *Mazzotti and Rajendran*, 2013]. This framework has been used successfully to describe reactive transport of multiple, interacting components in complex, natural porous media both in laboratory experiments and field applications [*Pope et al*., 1978; *Valocchi et al*., 1981; *Appelo and Postma*, 2010; *Venkatraman et al*., 2014].

In the geological sciences, the full chromatographic theory has primarily been used to describe infiltration metasomatism. *Korzhinskii* [1965, 1968] was the first to recognize the importance of chromatographic separations and reaction fronts during metasomatism. The work of Korzhinskii considered classical dissolution-precipitation reactions between multiple pure mineral phases and an aqueous solution. *Hofmann* [1972] applied chromatographic theory to binary ion exchange in feldspars and *Sedqui and Guy* [2001] explored ternary ion exchange during the formation of scarn garnets.

While studies of metasomatism considered the nonlinear interactions between major elements, most chromatographic work on melt migration in the mantle, starting with *Navon and Stolper* [1987], focuses on the transport of trace elements of variable compatibility at constant melt fraction (see among others *DePaolo* [1996], *Hauri and Kurz* [1997], and *Hauri* [1997]). This leads to a linear and decoupled system of equations that predicts a reduction of the transport velocity for trace elements with increasing compatibility in the solid phases. However, to understand nonlinear feedbacks such as the localization of melt flow into high-porosity channels, previous work must be extended to include the coupling between energy and mass transfer along with the interactions of major elements during reactive melt transport. While some studies consider porosity changes across reaction fronts, these changes are imposed rather than allowed to emerge as a consequence of the reactive melt transport itself [*Godard et al*., 1995].

This contribution extends the chromatographic analysis of reactive melt transport to major elements. In this case, the coupling between energy and mass transport is described by a phase diagram, and porosity evolves dynamically. Mass transfer between solid and melt may be compositionally or thermally driven during reactive melt transport. For purpose of illustration, an ideal binary solid solution liquid solution is considered, which yields a system of two nonlinear, coupled, hyperbolic partial differential equations. The analysis is presented as follows: section 2 introduces the nonlinear system of algebraic equations that determines the thermodynamic state of the system; section 3 introduces the partial differential equations describing the transport of energy and mass during reactive melt transport; section 4 presents the chromatographic analysis that forms the central contribution of this study; section 5 shows that the one-dimensional analysis predicts the stability of reaction fronts in higher dimensions and discusses geological applications.

2. Thermodynamic State Equations

Any reactive transport model requires a set of thermodynamic equations that determine the intensive state of the system and conservation equations that determine the extensive state of the system. Together they form a nonlinear system of algebraic equations that contain the key nonlinearities, couplings, and feedbacks during reactive melt transport. This section introduces these state equations and the phase space used to analyze the reactive transport behavior in section 4. The full description of the state of the system

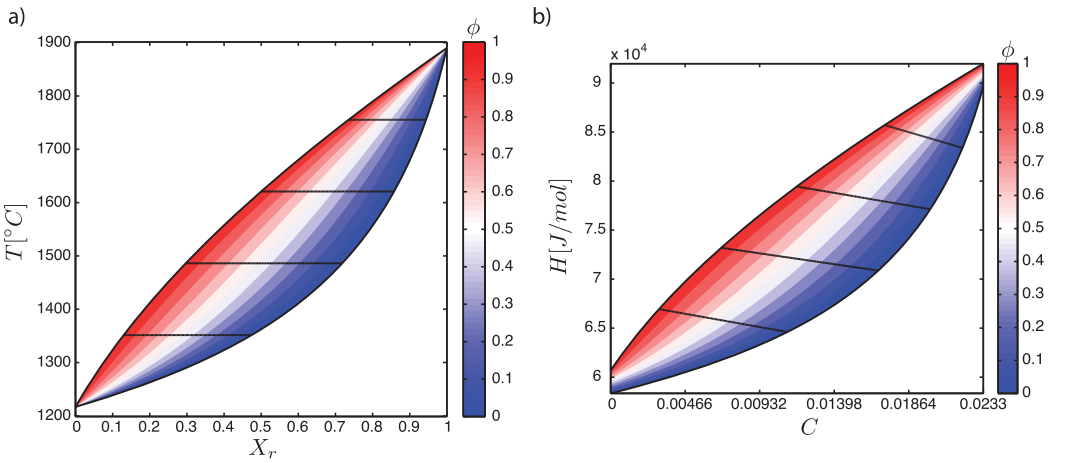

Figure 1. (a) Binary phase diagram for an ideal solid solution liquid solution, showing the two-phase region bound from below by the solidus $X_s(T)$ and above by the liquidus $X_l(T)$. Porosity, ϕ, is shown by the color map, and the black lines show the tie lines of constant temperature, T, in °C. X_r is the mole fraction of the refractory end-member. (b) The same phase diagram plotted in the phase space formed by the conserved quantities, bulk composition, C, and bulk enthalpy, H. Isothermal tie lines for T_f and T_r at each end of the phase diagram are vertical.

requires phase relations introduced in section 2.1, the equations describing the partitioning of the energy between phases in section 2.2, and the conservation equations given in section 2.3. Finally, a simplified set of state equations, comparable to those used in previous literature, is introduced and its properties are discussed in section 2.4. This system will subsequently be used in the analysis of reactive melt transport.

2.1. Ideal Binary Solid Solution Phase Behavior

Following previous work in melt migration, an ideal binary solid solution liquid solution is assumed that may represent the olivine solid solution in the mantle systems and the plagioclase solid solution in crustal systems [*Katz*, 2008; *Hewitt*, 2010; *Rudge et al*., 2011; *Solano et al*., 2014]. The component with the lower melting point, T_f, is referred to as the fusible component and denoted by the subscript f and the component with the higher melting point, T_r, is termed refractory and indicated by the subscript r. All expressions below are given in terms of the mole fractions of the refractory component in the melt, $X_{m,r} \equiv X_m$, and in the solid, $X_{s,r} \equiv X_s$. The mole fractions of the fusible components can be obtained from the mole fraction constraint in each phase, so that $X_{s,f} = 1 - X_s$ and $X_{m,f} = 1 - X_m$.

The standard formulation of an ideal solid solution liquid solution phase loop is chosen here to demonstrate the applicability of the analysis to proper thermodynamic descriptions of phase behavior. In this case, the dependence of melt and solid composition on temperature, T, are given by

$$X_m = \frac{1 - e^{-\Delta G_r/(2RT)}}{e^{-\Delta G_f/(2RT)} - e^{-\Delta G_r/(2RT)}}, \tag{1}$$

$$X_s = \frac{\left(1 - e^{-\Delta G_r/(2RT)}\right) e^{-\Delta G_f/(2RT)}}{e^{-\Delta G_f/(2RT)} - e^{-\Delta G_r/(2RT)}}, \tag{2}$$

and referred to as the liquidus and solidus curves that bound the two-phase region. Here R is the universal gas constant. The Gibbs free energy of fusion of the fusible and refractory end-members ΔG_f and ΔG_r are described by equations (A1)–(A9) in Appendix A. The resulting phase diagram is modeled after the olivine solid solution, shown in Figure 1a. The parameter values used are given in Table 1. The stoichiometry of the olivine reaction accounts for the factor of 2 in the exponents in (1) and (2).

In previous work on trace element transport, the relationship between solid and melt composition is linear, $X_s = K_d X_m$, although K_d may vary with time as a function of pressure and temperature [*White*, 2013]. This relation is nonlinear for major elements and variations in pressure and temperature cannot be separated from composition. In the case of ideal solid solution liquid solution discussed here, the relationship between X_s and X_m is monotonic and convex, $\mathrm{d}^2 X_s / \mathrm{d} X_m^2 \neq 0$, if $T_r > T_f$. The treatment of the nonlinearity in major element phase

behavior in the chromatographic analysis of the reactive melt transport is one of the main advances in this contribution.

2.2. Enthalpies in an Ideal Solid Solution

In an ideal binary solid solution, the specific enthalpy of the solid is the mechanical mixture of the specific enthalpies of the two end-members

$$h_s = X_s\, h_{sr}(T) + (1 - X_s)\, h_{sf}(T), \tag{3}$$

which are linear functions of T and given in Appendix B. The specific enthalpy of the melt is that of the solid phase plus the specific latent heat of fusion

$$h_m = h_s + \Delta H. \tag{4}$$

The latent heat of fusion in an ideal solid solution liquid solution system is the mechanical mixture of the specific latent heats of fusion of the two end-members

$$\Delta H = X \Delta H_r(T) + (1 - X)\, \Delta H_f(T), \tag{5}$$

which are also linear functions of T and given in Appendix B. Here X is the total mole fraction of the refractory component in the partially molten system given by

$$X = F X_m + (1 - F) X_s, \tag{6}$$

where F is the mole fraction of the melt.

2.3. Conserved Quantities

The thermodynamic equations above determine the intensive state of the system and are sufficient to determine the equilibrium state of the system. However, reactive melt transport requires knowledge of the proportions of the phases. Due to mass and energy transfer between phases during reactive melt transport, the conserved quantities are the total moles of the refractory component in the system, C, and the total enthalpy of the system, H. These quantities are per unit volume. Therefore, they depend on the molar densities, ρ_m and ρ_s, and the volume fraction of the melt, ϕ. Thus, conserved quantities are given by

$$C = \rho_m \phi X_m + \rho_s (1 - \phi) X_s, \tag{7}$$

$$H = \rho_m \phi h_m + \rho_s (1 - \phi) h_s, \tag{8}$$

where the pore space is saturated with melt. The porosity is related to the mole fraction of the melt as follows

$$F = \frac{\phi \rho_m}{\phi \rho_m + (1 - \phi) \rho_s}. \tag{9}$$

The conserved quantities C and H form a phase space that allows a two-dimensional representation of all model states. At any point within this phase space, (6)–(9) form a closed system of four nonlinear algebraic equations for the four unknowns T, X, F, and ϕ. Once these primary variables are known all other model quantities can be determined.

2.4. Simplified Model Equations

For clarity of presentation, a simplified system, similar to those presented in the recent literature [*Katz*, 2008; *Hewitt*, 2010; *Solano et al.*, 2014], is considered for the analysis below.

Table 1. Simplified Model Thermodynamic Properties Based on the Olivine Solid Solution Liquid Solution

Parameter	Value	Units
T_r	1890	°C
T_f	1217	°C
$\Delta H_r = \Delta H_f = L$	100	kJ/mol
h_0	250	kJ/mol
ρ	2.33×10^{-2}	mol/cm^3
c_p	2	kJ/K/mol

In the limit where all phases have the same constant density, ρ, equation (9) simplifies to $F = \phi$, so that $C = \rho X$. In section B4, we show that latent heat of fusion becomes constant, $\Delta H = L$, in the limit where all enthalpic properties are constant and equal across phases and end-members. After applying these simplifications, the expressions for conserved quantities are given by,

$$C=\rho(\phi X_m+(1-\phi)X_s), \tag{10}$$

$$H=\rho\left(h_0+c_p(T-T_0)+\phi L\right). \tag{11}$$

In the simplified expression for enthalpy, (11), c_p is the specific molar heat capacity and h_0 is specific enthalpy at the reference temperature, T_0.

The simplified model equations (10) and (11) form a closed system for T and ϕ given C and H. This allows the reduction of the state equations to a single nonlinear equation for T. Equation (10) is rearranged for ϕ and substituted into (11) yielding

$$R(C,H,T)=(C-\rho X_s(T))L+(h_s(T)-H)(X_m(T)-X_s(T))=0. \tag{12}$$

Equation (12) cannot be inverted for T explicitly, but it can be solved robustly and efficiently using a one-dimensional root finding method. Once the temperature of the system is known ϕ can be obtained from (10). Figure 1b shows the variation of T and ϕ in two-phase region of the CH-phase space.

3. Transport Model

In a reference frame moving with the solid phase, the conservation equations are given by

$$C_t+\nabla\cdot(\mathbf{q}\rho X_m-\phi\rho D\nabla X_m)=0, \tag{13}$$

$$H_t+\nabla\cdot\left(\mathbf{q}\rho h_m-\rho\bar{k}\nabla T\right)=0, \tag{14}$$

where $\mathbf{q}$ is the volumetric melt flux relative to the solid given by Darcy's law, and the subscript, t, denotes the time derivative. Diffusion in the solid has been neglected in (13), and D is the effective hydrodynamic dispersion of the porous medium. The average thermal conductivity of the medium is given by $\bar{k}=(\phi/\vartheta)k_m+(1-\phi)k_s$, where ϑ is the tortuosity, and k_m and k_s are the thermal conductivities in the solid and the melt.

The equations are recast in terms of dimensionless variables

$$\mathcal{C}=\frac{C}{\rho},\quad \mathcal{T}=\frac{T-T_f}{T_r-T_f},\quad \zeta=\frac{x}{\ell},\quad \text{and}\quad \tau=\frac{tq}{\ell}, \tag{15}$$

where $q=|\mathbf{q}|$, which is given and constant in one dimension. These scales imply the following expression for dimensionless enthalpy

$$\mathcal{H}=\frac{H-\rho h_s^{T_f}}{\rho c_p\Delta T}. \tag{16}$$

For the initial condition considered below, the reactive melt transport problem does not contain an intrinsic length scale. Here the spatial coordinate, x, is normalized by the dimension of the heterogeneity, ℓ.

The dimensionless conserved quantities simplify to

$$\mathcal{C}=\phi X_m(\mathcal{T})+(1-\phi)X_s(\mathcal{T}), \tag{17}$$

$$\mathcal{H}=\mathcal{T}+\frac{\phi}{\mathrm{Ste}}, \tag{18}$$

where the ratio of sensible heat to latent heat is the Stefan number, $\mathrm{Ste}=c_p(T_r-T_f)/L$. Equation (18) is rearranged for ϕ and substituted into (17) giving the dimensionless equation of state,

$$\mathcal{F}(\mathcal{C},\mathcal{H},\mathcal{T})=\mathcal{C}+\mathrm{Ste}(\mathcal{H}-\mathcal{T})[X_s(\mathcal{T})-X_m(\mathcal{T})]-X_s(\mathcal{T})=0. \tag{19}$$

The dimensionless conservation laws for composition and enthalpy are

$$\mathcal{C}_\tau+\nabla\cdot(X_m-Pe_{\mathcal{C}}^{-1}\phi\nabla X_m)=0, \tag{20}$$

$$\mathcal{H}_\tau+\nabla\cdot(f_m-Pe_{\mathcal{H}}^{-1}(\phi+\kappa(1-\phi))\nabla\mathcal{T})=0, \tag{21}$$

where $\kappa=k_s\vartheta/k_l$ and the Péclet numbers are given by $Pe_{\mathcal{C}}=q\delta/D$ and $Pe_{\mathcal{H}}=q\vartheta\delta/k_l$. Note that ϕ has not been absorbed into the Péclet numbers because it evolves dynamically and may even vanish. Here the dimensionless enthalpy of the melt is given by

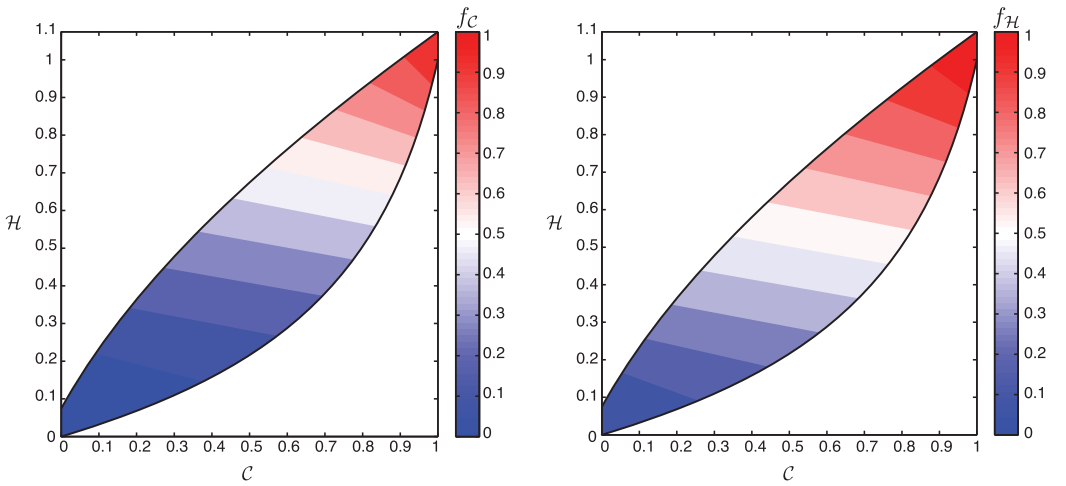

Figure 2. (a) The dimensionless flux of composition, given by $f_{\mathcal{C}}=X_m$, in the $\mathcal{CH}$ phase space. (b) The dimensionless flux of enthalpy, given by $f_{\mathcal{H}}=\mathit{fi}_m$.

$$\mathit{fi}_m=\mathcal{T}+\mathrm{Ste}^{-1}. \tag{22}$$

Details of the nondimensionalization of enthalpy can be found in Appendix C.

In reactive melt transport, advection dominates diffusion [*Aharonov et al.*, 1995; *Katz*, 2008; *Hesse et al.*, 2011]. Therefore, the analysis below considers the limit of $Pe_{\mathcal{C}} \to \infty$ and $Pe_{\mathcal{H}} \to \infty$. In this limit, the governing equations reduce to a quasi-linear system of coupled hyperbolic equations

$$\mathbf{u}_\tau+\nabla\cdot\mathbf{f}(\mathbf{u})=0. \tag{23}$$

Here $\mathbf{u}=[\mathcal{C},\ \mathcal{H}]$ is the vector of conserved quantities and $\mathbf{f}(\mathbf{u})=[X_m,\ \ \mathit{fi}_m]$ is their nonlinear flux vector. These fluxes are shown in Figure 2 and represent the amount of material and energy that can be transported by the melt. It should be noted that the solutions to (23) are weak solutions that may contain discontinuities, where the derivatives are not defined and require a suitable entropy condition to guarantee uniqueness [*LeVeque*, 1991].

4. Melt Transport Across a Discontinuity

This section considers the reaction fronts that arise as melt flows across a discontinuity in composition and enthalpy as shown in Figure 3a. The essential behavior of these problems can be understood by a one-dimensional analysis. Section 5 will discuss how higher-dimensional phenomena such as the occurrence of melt localization can be deduced from the one-dimensional analysis.

4.1. General Structure of Reaction Fronts

Consider the following one-dimensional initial value problem commonly referred to as a Riemann problem

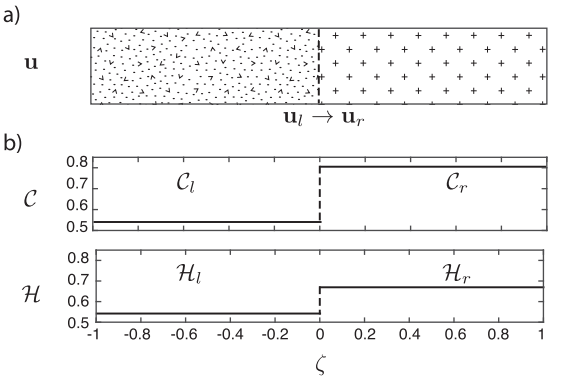

Figure 3. (a) Schematic representation of **u** across a lithological discontinuity. (b) Initial conditions for the Riemann problem for conserved variables $\mathcal{C}$ and $\mathcal{H}$ plotted against dimensionless spatial coordinate ζ.

$$\mathbf{u}_\tau+\mathbf{f}(\mathbf{u})_\zeta=0,\quad \zeta\in \mathrm{R} \tag{24}$$

$$\mathbf{u}=\begin{cases}\mathbf{u}_l, & \zeta<0,\\ \mathbf{u}_r, & \zeta>0.\end{cases} \tag{25}$$

Subscripts *l* and *r* refer to left and right states of enthalpy and concentration. This nomenclature is commonly used in theory of hyperbolic conservation laws [*LeVeque*, 1991]. In the analysis that follows, the flow always traverses from left to right such that $q>0$. The initial condition is illustrated in Figure 3b.

The solution of the Riemann problem for well-behaved systems of two coupled quasi-linear equations is characterized by the

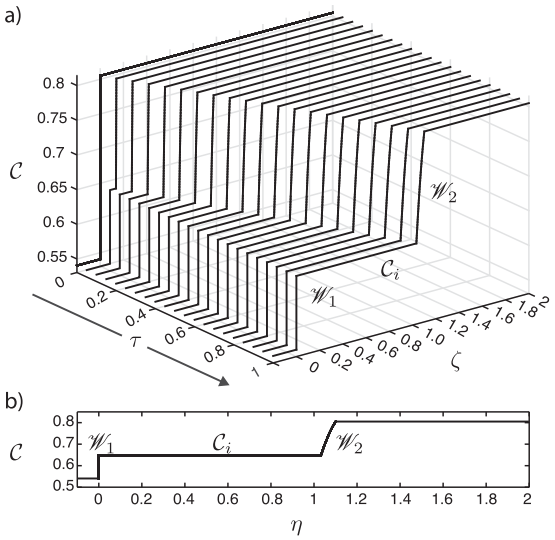

Figure 4. (a) Evolution of the dimensionless total concentration in ζ and τ. (b) The same solution plotted as function of similarity variable, $\eta=\zeta/\tau$.

formation of an intermediate state, $\mathbf{u}_i$, bounded by two waves $\mathscr{W}_1$ and $\mathscr{W}_2$ [*LeVeque*, 1991]. This solution structure evident in Figure 4 and can be represented as follows

$$\mathbf{u}_l \xrightarrow{\mathscr{W}_1} \mathbf{u}_i \xrightarrow{\mathscr{W}_2} \mathbf{u}_r. \tag{26}$$

In the context of reactive melt transport, the waves are reaction fronts and the intermediate state corresponds to a reacted zone that forms between the fronts.

The system of nonlinear hyperbolic equations can be written in quasi-linear form,

$$\mathbf{u}_\tau + \nabla_{\mathbf{u}}\mathbf{f}(\mathbf{u})\mathbf{u}_\zeta = 0, \tag{27}$$

where gradient of the flux with respect to the conserved quantities is given by

$$\nabla_{\mathbf{u}}\mathbf{f}(\mathbf{u}) = \begin{pmatrix} f_{\mathcal{C},\mathcal{C}} & f_{\mathcal{C},\mathcal{H}} \\ f_{\mathcal{H},\mathcal{C}} & f_{\mathcal{H},\mathcal{H}} \end{pmatrix}. \tag{28}$$

Within the two-phase region, the derivatives of the flux gradient above can be evaluated through implicitly differentiating the function $\mathcal{F}(\mathcal{C},\mathcal{H},\mathcal{T})$, see Appendix D1. Equation (27) is a system of advection equations where the propagation velocity is determined by the flux gradient. The flux gradient itself only depends on **u**. Figure 4a shows the development of reaction fronts emerging in a typical Riemann problem. The pattern of reaction fronts remains the same through time, because each reaction front moves with its own characteristic velocity. Essentially, solution profiles stretch with time.

4.2. Self-Similarity of Reaction Fronts

The recognition of the constant, stretching morphology of the reaction fronts allows the introduction of the similarity variable

$$\eta = \zeta/\tau. \tag{29}$$

Physically, η describes the dimensionless propagation velocity of the reaction fronts. Figure 4b shows that the solution collapses to a single profile when plotted as function of η. This suggests that the system of partial differential equations, given by (24), can be reduced to a system of ordinary differential equations given by

$$\left(\nabla_u\mathbf{f} - \lambda_p\mathbf{I}\right)\frac{\mathrm{d}\mathbf{u}}{\mathrm{d}\eta} = \left(\mathbf{A} - \lambda_p\mathbf{I}\right)\mathbf{r}_p = 0, \quad p \in [1, 2]. \tag{30}$$

This system of two differential equations can be thought of as a nonlinear eigenvalue problem, where the eigenvalues λ_1 and λ_2 are the characteristic propagation speeds of $\mathscr{W}_1$ and $\mathscr{W}_2$, respectively. The associated eigenvectors $\mathbf{r}_p = \mathrm{d}\mathbf{u}/\mathrm{d}\eta$ give pathways through $\mathcal{CH}$ phase space that satisfy the conservation equations.

Any constant sate **u** satisfies $\mathrm{d}\mathbf{u}/\mathrm{d}\eta = 0$ and is a trivial solution to (30). Continuous solutions to (30) must satisfy the eigenvalue problem,

$$\left(\mathbf{A} - \lambda_p\mathbf{I}\right)\mathbf{r}_p = 0. \tag{31}$$

The propagation velocity of discontinuities in the solution must satisfy the Rankine-Hugoniot jump condition

$$\Lambda_p(\mathbf{u}_+, \mathbf{u}_-) = \frac{\mathbf{f}(\mathbf{u}_+) - \mathbf{f}(\mathbf{u}_-)}{\mathbf{u}_+ - \mathbf{u}_-} = \frac{[\mathbf{f}(\mathbf{u})]}{[\mathbf{u}]}, \tag{32}$$

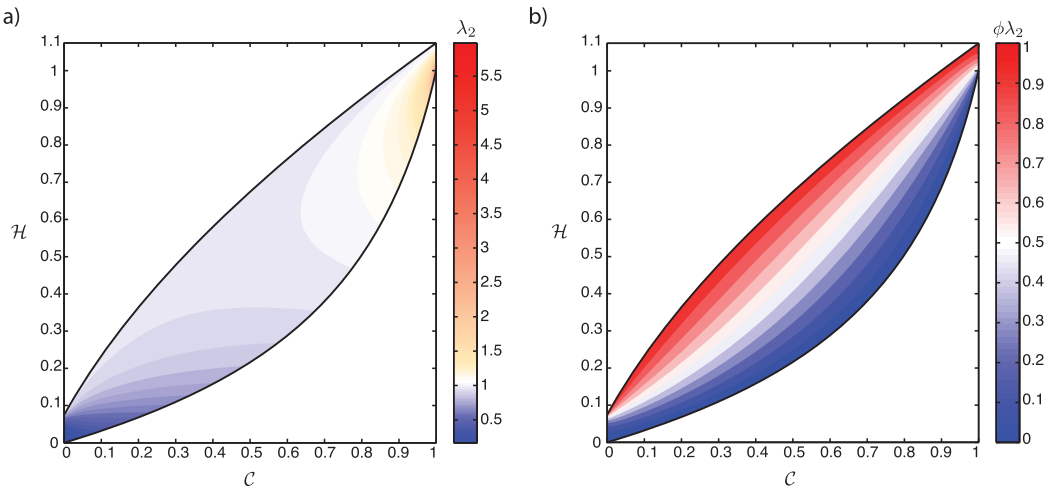

Figure 5. (a) The eigenvalue λ_2 in the two-phase region. (b) The scaled eigenvalue $\phi\lambda_2$, associated with propagation speed of the reaction fronts relative to the average melt velocity.

which arises from mass balance around the discontinuity [*LeVeque*, 1991]. This condition can be thought of as a discrete version of the eigenvalue problem (31). Here $\mathbf{u}_-$ is the state to the left of the discontinuity and $\mathbf{u}_+$ is the state to the right, so that the notation $[\cdot]$ indicates the jump across the discontinuity. The values for $\mathbf{u}_-$ and $\mathbf{u}_+$ describe the immediate vicinity of the moving discontinuity and are not necessarily the same as $\mathbf{u}_l$ and $\mathbf{u}_r$ as they may refer to the intermediate state, $\mathbf{u}_i$.

4.3. Construction of Solution Grid in $\mathcal{CH}$ Space

The self-similar solutions are constructed by identifying directions in $\mathcal{CH}$ phase space that satisfy the conservation laws and the equation of state. One such set of directions that allows reaction fronts with continuous variations in $\mathbf{u}$ is obtained by integrating the eigenvectors. Another set of directions is determined by the nonlinear algebraic system of equations arising from the jump condition (32) and describes discontinuous reaction fronts [*LeVeque*, 1991].

The eigenvalues of (31) are given by,

$$\lambda_1 = 0 \quad \text{and} \quad \lambda_2 = f_{\mathcal{C},\mathcal{C}} + f_{\mathcal{H},\mathcal{H}}. \tag{33}$$

Figure 5a shows that λ_2 is nonnegative and increases monotonically in the direction of increasing $\mathcal{C}$ and has a maximum at the solidus of the refractory end-member. The eigenvalue, λ_p, gives the dimensionless propagation speed of the reaction front, $\mathscr{W}_p$, as a function of $\mathcal{C}$ and $\mathcal{H}$. The first reaction front, $\mathscr{W}_1$, is stationary because $\lambda_1 = 0$. Therefore, all solutions have a single moving reaction front. Due to variable porosity, the dimensionless system is scaled with respect to the constant volumetric flux, q, rather than the variable melt velocity. Hence the propagation speed of the second reaction front relative to the melt is $\phi\lambda_2$, as shown in Figure 5b. As expected, the propagation velocities relative to the melt are significantly retarded near the solidus.

The corresponding eigenvectors yield two linearly independent directions in $\mathcal{CH}$ phase space

$$\mathbf{r}_1 = \begin{pmatrix} -\dfrac{\partial \mathcal{C}}{\partial \mathcal{H}} \\ 1 \end{pmatrix} \quad \text{and} \quad \mathbf{r}_2 = \begin{pmatrix} \dfrac{\mathrm{d}X_m}{\mathrm{d}\mathcal{T}} \\ 1 \end{pmatrix}, \tag{34}$$

that can be integrated

$$\mathbf{u}(\mathbf{u}_0, \eta) = \mathbf{u}_0 + \int_0^{\eta} \mathbf{r}_p \mathrm{d}\eta', \tag{35}$$

to obtain solution pathways. These paths in $\mathcal{CH}$ phase space comprise the set of states that can be connected to $\mathbf{u}_0$ by a reaction front with a continuous variation in $\mathbf{u}$. Figure 6a illustrates solutions to the

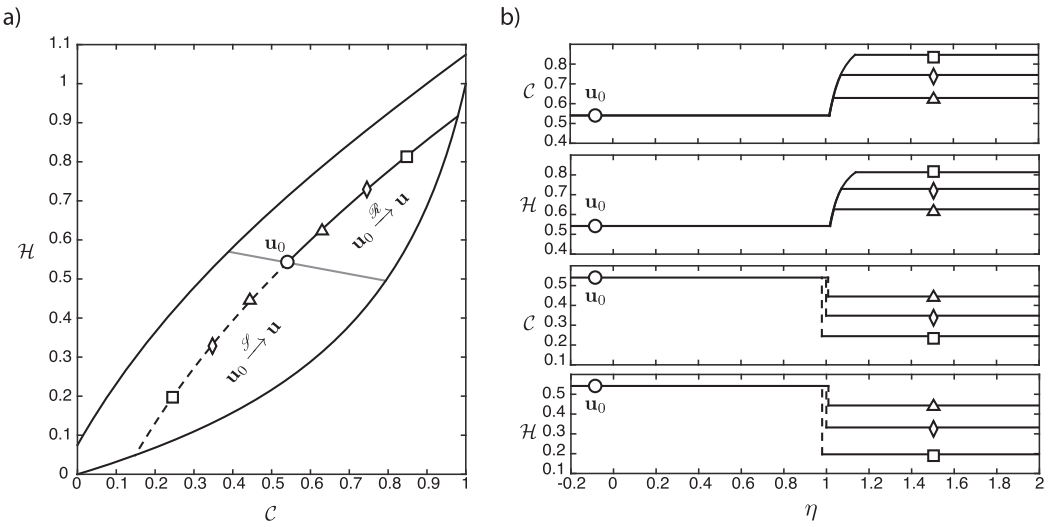

Figure 6. (a) Integral curve (line) and Hugoniot-locus (dotted line) associated with a left state given by $\mathbf{u}_0$. (b) Rarefaction fronts for three states along the integral curve. (c) Shock fronts for three states along the Hugoniot-locus.

eigenvalue problem at a particular state, $\mathbf{u}_0$. The discussion below assumes that $\mathbf{u}_0$ is a left state, $\mathbf{u}_l$, and describes the set of permissible right states, $\mathbf{u}_r$.

4.3.1. Stationary Linear Reaction Front

The integral curves associated with λ_1 and $\mathbf{r}_1$, known as the first characteristic field [*LeVeque*, 1991], are parallel to the isothermal tie lines of the phase diagram in $\mathcal{CH}$ phase space. Any right state, $\mathbf{u}_r$, along this integral curve, connected to $\mathbf{u}_0$ by a stationary discontinuity is a weak solution of (24). Because the λ_1 is constant, the first characteristic field is linearly degenerate and the stationary front is referred to as a contact discontinuity, $\mathscr{C}_1$. This front is stationary, because the composition and enthalpy of the melt are soley functions of temperature and hence identical on either side of an isothermal contact. Therefore, fluxes of $\mathcal{C}$ and $\mathcal{H}$ (Figure 2) are constant so that melt transport does not change $\mathcal{C}$ and $\mathcal{H}$ and the front does not evolve.

The importance of tie lines in the solution construction of multicomponent systems has been observed for multiphase flow with partitioning in gas-liquid [*Welge et al*., 1961] and liquid-liquid [*Wachmann*, 1964] systems. See *Orr* [2005] for a comprehensive review. In general, the recovery of the single-component solution from the multicomponent system requires that tie lines are solution paths.

4.3.2. Moving Nonlinear Reaction Front

The integral curves associated with the second characteristic field mimic the shape of the liquidus because they are obtained by integrating $\mathrm{d}X_m/\mathrm{d}\mathcal{T}$. Since λ_2 varies smoothly, any $\mathbf{u}$ along this integral curve is connected to $\mathbf{u}_0$ by a continuously varying reaction front. The propagation velocity along these continuous reaction fronts increases monotonically such that the reaction front spreads with time. These fonts are referred to as rarefactions and denoted $\mathscr{R}_2$. Rarefactions are a weak solution of (30) if the resultant profile of $\mathbf{u}$ is single valued. This condition is satisfied if $\mathbf{u}$ lies on the branch of the integral curve emanating from $\mathbf{u}_0$ in the direction of increasing λ_2 toward the refractory end-member, as shown in Figure 6a. Examples of rarefaction profiles corresponding to a sequence of right states along the integral curve are shown in Figure 6b.

If $\mathbf{u}$ lies on the opposite branch of the integral curve, a continuous reaction front would result in unphysical triple-valued solutions. In this case, $\mathbf{u}$ is connected to $\mathbf{u}_0$ by a discontinuous reaction front that propagates with a velocity, $\Lambda_2(\mathbf{u}_0, \mathbf{u})$, set by the jump condition. Such fronts are referred to as shocks and are denoted, $\mathscr{S}_2$. The set of permissible $\mathbf{u}$ that can be connected to $\mathbf{u}_0$ by shocks lie on the segment of the Hugoniot-locus that satisfies the entropy condition. The Hugoniot-locus is obtained by solving the two nonlinear algebraic equations given by (32) for the two components of $\mathbf{u}$ and Λ_2. For the system of equations discussed here, the Hugoniot-locus is visually indistinguishable from the integral curve. The segment that satisfies the entropy condition lies on the branch of the Hugoniot-locus emanating from $\mathbf{u}_0$ in the direction of decreasing λ_2 toward the fusible end-member, as shown in Figure 6a. Examples of shock profiles corresponding to a sequence of states along the Hugoniot-locus are shown in Figure 6c.

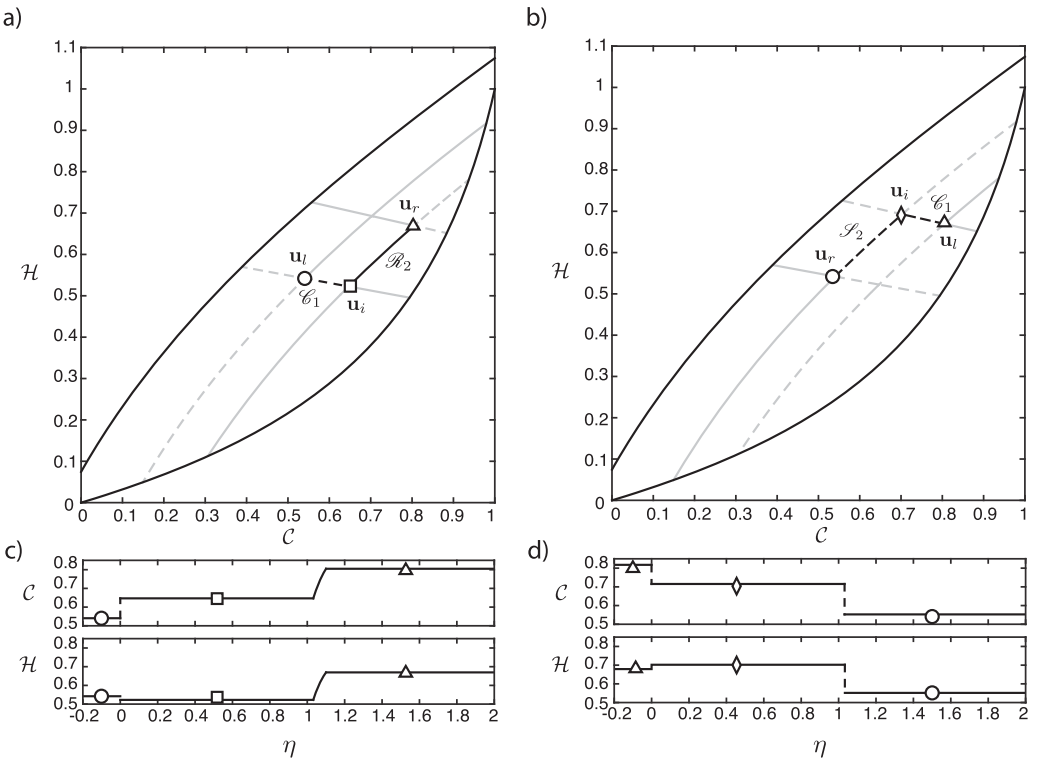

Figure 7. (a and b) The intermediate state, $\mathbf{u}_i$, formed by the intersection of the integral curves (line) and Hugoniot-loci (dotted line) associated with $\mathbf{u}_l$ and $\mathbf{u}_r$. Solution paths are shown in black. (c and d) Self-similar profiles corresponding to solution paths shown in Figures 7a and 7b.

The previous analysis searched for connected states, $\mathbf{u}$ assuming that the given a state, $\mathbf{u}_0$, is a left state, $\mathbf{u}_l$. The same arguments show that the location of the integral curve and the Hugonoit-locus are switched if the reference point $\mathbf{u}_0$ is a right state.

4.3.3. Intermediate State: Formation of a Reacted Zone

The solution profile contains a single reaction front if $\mathbf{u}_l$ and $\mathbf{u}_r$ share the same integral curve or Hugonoit-locus. In all other cases, a reacted zone forms, which is represented in $\mathcal{CH}$ phase space as an intermediate state, $\mathbf{u}_i$. At this intermediate state, the solution switches from the first characteristic field to the second (Figures 7a and 7b). In other words, at $\mathbf{u}_i$, the solution changes from the stationary front along isothermal tie lines to the advancing reaction front along the paths that mimic the liquidus.

The two possible intermediate states are given by the intersections of the integral curves and Hugoniot-loci emanating from $\mathbf{u}_l$ and $\mathbf{u}_r$, as shown in Figure 7a. Only one intersection yields a physically realistic single-valued solution. The correct intersection is selected by requiring that the propagation speed increases monotonically from $\mathbf{u}_l$ to $\mathbf{u}_r$. Because $\lambda_1 \leq \lambda_2$, the integral curves and Hugoniot-loci associated with the first characteristic field are referred to as slow paths and those associated with the second characteristic field are termed fast paths. A single-valued solution is ensured if and only if $\mathbf{u}_l$ is connected to $\mathbf{u}_i$ along the slow path and $\mathbf{u}_i$ is connected to $\mathbf{u}_r$ along the fast path. The reactive melt transport system considered here allows only two fundamental solution structures

$$\mathbf{u}_l \xrightarrow{\mathscr{C}_1} \mathbf{u}_i \xrightarrow{\mathscr{R}_2} \mathbf{u}_r \quad \text{and} \quad \mathbf{u}_l \xrightarrow{\mathscr{C}_1} \mathbf{u}_i \xrightarrow{\mathscr{S}_2} \mathbf{u}_r, \tag{36}$$

because the first characteristic is linearly degenerate and the reaction front along the slow path is always a contact discontinuity.

The reactive melt transport across an initial discontinuity is characterized by the formation of a reacted zone corresponding to $\mathbf{u}_i$ that is bounded between a stationary front, $\mathscr{C}_1$, and an advancing front that is either a spreading rarefaction front, $\mathscr{R}_2$, as illustrated in Figures 7a and 7c or a shock, $\mathscr{S}_2$, as illustrated in

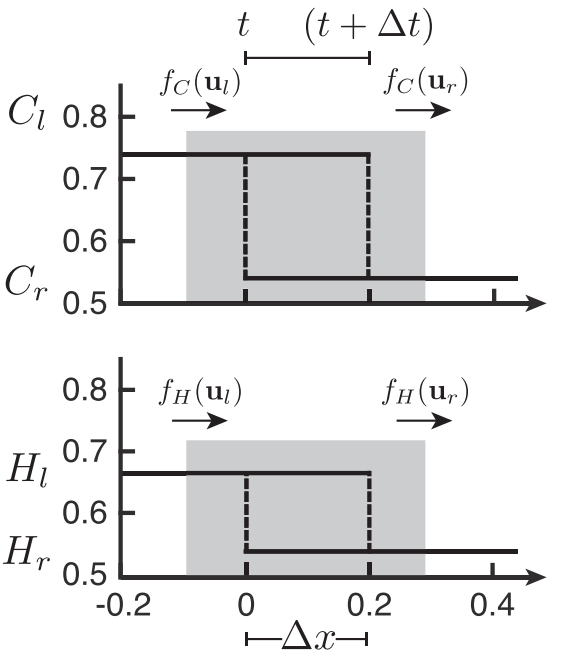

Figure 8. Mass and energy balances across a moving reaction front considered in (37). Control volume over which balance is considered is shown in gray. Reaction front moves distance Δx over time interval Δt.

Figures 7b and 7d. The transient solution in Figure 4 is equivalent to the self-similar solution profiles in Figure 7c.

5. Discussion

The analysis of reactive melt transport across an initial discontinuity presented above leads to multiple important insights and their implications are discussed below. Section 5.1 gives the physical interpretation of the different fronts that arise in reactive melt transport. Section 5.2 shows that the entire reactive melt transport behavior can be summarized graphically, which leads to a regime diagram that identifies unstable reaction fronts that localize the melt flow as well as self-limiting fronts that cut off the flow.

5.1. Physical Interpretation of Reaction Fronts

This section complements the mathematical analysis presented in section 4 with physical interpretation of the different behavior of the reaction fronts. The analysis identified stationary isothermal fronts (contact discontinuities), moving discontinuous fronts (shocks), and moving fronts that widen with time (rarefactions).

5.1.1. Stationary Isothermal Fronts: Contact Discontinuities

The formation of the isothermal stationary front, $\mathscr{C}_1$, at the location of the initial interface may be counterintuitive. This is best understood through a physical interpretation of the jump condition (32) that determines the velocity of sharp reaction fronts. Figure 8 shows that the jump condition can be thought of as a mass balance on a control volume around the moving front. The motion of the reaction front is the manifestation of a change in bulk composition or bulk enthalpy or both in its vicinity. Such changes are due to a imbalance in the composition and enthalpy fluxes across the front.

For example, consider the change in bulk composition across the contact discontinuity pictured in Figure 8. The change in mass of the refractory component within the control volume due to the migration of the reaction front by distance Δx is given by $\Delta M = A\Delta x(C_L - C_R)$, where A is a unit cross-section perpendicular to the direction of flow. This change in mass is due to the difference in the mass flux on the left and right boundaries of the control volume so that

$$A\Delta x(C_l - C_r) = qA\Delta t(f_C(\mathbf{u}_l) - f_C(\mathbf{u}_r)), \tag{37}$$

where Δt is the time interval over which the change occurs. This mass balance can be solved for the propagation speed of the front, given by

$$\frac{\Delta x}{\Delta t} = q\left(\frac{f_C(\mathbf{u}_l) - f_C(\mathbf{u}_r)}{C_l - C_r}\right). \tag{38}$$

Together with a similar balance for enthalpy across the front and suitable nondimensionalization, this leads to the jump condition for propagation speed of the reaction front (32).

Within this context, consider two rocks of different bulk composition that are separated by an isothermal discontinuity. They both lie along the same tie line and must have the same melt composition and enthalpy in melt. As energy and mass are only transported by the melt phase, the fluxes, f_C and f_H, are constant across the discontinuity (Figure 2), so that frontal velocity is zero according to the jump condition (38).

5.1.2. Ion Exchange at Nonlinear Moving Fronts

The moving reaction front, $\mathscr{W}_2$, can either be a sharp shock, $\mathscr{S}_2$, or a spreading rarefaction, $\mathscr{R}_2$. This type of behavior is well known for reactive transport with surface reactions such as adsorption-desorption or ion exchange [*DeVault*, 1943; *Glueckauf*, 1945; *Rhee et al*., 1970; *Mazzotti and Rajendran*, 2013]. Rarefactions have not been described for classical reactions with porosity change [*Korzhinskii*, 1968; *Bryant et al*., 1987; *Walsh et al*., 1984]. A particular challenge in the description of reactive melt transport in binary systems with solid solution liquid solution is the coupling ion exchange, heat transfer, and porosity change.

In the absence of porosity change, (20) reduces to the retardation equation typically written as follows,

$$R(X_m)\frac{\partial X_m}{\partial \tau}+\frac{\partial X_m}{\partial \zeta}-\mathrm{Pe}_{\mathcal{C}}^{-1}\frac{\partial^2 X_m}{\partial \zeta^2}=0, \tag{39}$$

where the retardation is given by

$$R(X_m)=\phi+(1-\phi)\frac{\mathrm{d}X_s}{\mathrm{d}X_m}. \tag{40}$$

The relationship between X_s and X_m is determined by the phase behavior. For sufficiently dilute concentrations, Henry's law applies, so that $X_s = K_d X_m$. In this limit, the retardation equation reduces to the linear equation for trace element transport given by *Navon and Stolper* [1987]. The propagation velocity of a trace element relative to the melt velocity is controlled solely by its partition coefficient. From (40), it can be seen that retardation increases linearly with K_d so that compatible trace elements lag behind incompatible trace elements.

Nonlinear retardation equations also describe the equilibrium transport of major cation species in groundwater in the presence of ion exchange with sorbed species on the solid surface [*Appelo and Postma*, 2010]. Here the aqueous concentration is analogous to the melt mole fraction, $c_{aq} \sim X_m$, and the sorbed concentration is analogous to the solid mole fraction, $c_s \sim X_s$. During contaminant transport, concentrations are often high enough that a nonlinear relationship between sorbed and aqueous concentrations must be considered. Since the temperature is often constant in environmental applications, the relationship between sorbed and aqueous concentrations is referred to as an isotherm [*Rhee et al*., 1989; *Mazzotti and Rajendran*, 2013].

For nonlinear isotherms, the retardation is strongly dependent on the concentration which gives rise to self-sharpening shocks and spreading reaction fronts. When a cation species is introduced into the groundwater, ion exchange with the solid retards its propagation speed in similar fashion to the retardation of a compatible trace element in melt transport. Adsorption fronts are self-sharpening because low concentrations ahead of the shock are retarded more strongly than high concentrations behind the shock. In contrast, desorption fronts spread with time because desorption becomes less favorable as concentration decreases.

A similar process occurs in reactive melt transport along the nonlinear moving front. The relation between the liquidus and solidus compositions, shown by the Roozeboom plot in Figure 9, determines whether the reaction front is spreading or self-sharpening in a similar manner to the ion exchange isotherm in contaminant transport applications [*Roozeboom*, 1899].

For the example of the olivine solid solution liquid solution, the Roozeboom plot illustrates that magnesium is preferentially incorporated into the solid while iron is enriched in the melt. Equation (40) shows that the retardation of the magnesium mole fraction in melt transport is proportional to the slope in the Roozeboom plot. Therefore, the transport speed, given by $1/R(X_m)$, increases with increasing magnesium mole fraction, as shown in Figure 5a. Furthermore, this dependence of the propagation speed on composition provides an intuitive explanation for the formation of shocks along the Hugonoit-locus and rarefactions along the integral curve as shown in Figure 6a.

5.2. Graphical Representation of Full Set of Solutions

The analysis presented in section 4 allows graphical representation of the complete set of solutions for reactive melt transport across a discontinuity in enthalpy and composition. Figure 9 shows a net of integral curves across the two-phase region of $\mathcal{CH}$ phase space. This net is composed of the slow paths that lie along isothermal tie lines and the fast paths that mimic the liquidus. For any left and right state, this

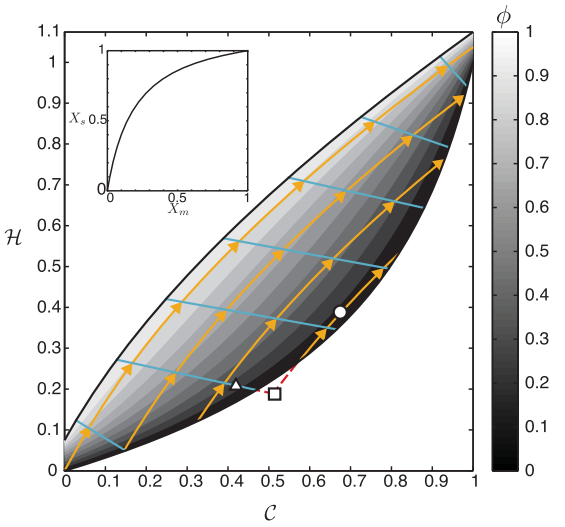

Figure 9. Porosity contours with net of solution paths demonstrating the solution structure. Solutions must first travel along the slow path (line) and then follow the fast path (arrow). Solutions that move in the direction of the arrows follow the integral curves and form rarefactions. Solutions that follow the Hugoniot-loci move against the arrows and form shocks. A hypothetical pathway for a self-limiting reaction front is shown (red dotted line). *Inlay*: Roozeboom diagram for olivine solid solution. The relationship between liquidus and solidus compositions along the Roozeboom diagram determine whether the reaction front is spreading or self-sharpening. For the case $X_s = K_d X_m$, the Roozeboom diagram is a straight line with slope K_d.

net allows the construction of the solution according to the wave structures given by (36). The intermediate state between the stationary and advancing reaction front lies at the intersection of the slow path emanating from the left state and the fast path emanating from the right state. The morphology of the advancing reaction front is determined by the direction of the solution along the fast path between the intermediate state and the right state. A spreading wave forms if the solution follows the arrows along the fast path in Figure 9, otherwise, a shock forms. The figure also allows for the prediction of porosity changes across reaction fronts by inspection.

5.2.1. Melting-Freezing Versus Dissolution-Precipitation

Porosity changes are induced both by dissolution-precipitation driven by changes in composition and melting-freezing driven by changes in enthalpy. A porosity change along a vertical solution path in $\mathcal{CH}$ space indicates pure melting, whereas a porosity change along a horizontal solution path indicates pure dissolution-precipitation. The slope of solution paths shown in Figure 9 demonstrates that porosity changes across both the stationary and the moving reaction fronts are induced by both processes. Pure melting and freezing only occurs in pure component systems. In this limit, the dynamics can be described by enthalpy balance alone, and there is a single stationary front along the vertical slow paths corresponding to the T_r and T_f isotherms of the solution grid in Figure 9. Although there are vertical pathways in $\mathcal{CH}$ space at end-members, there are no horizontal pathways. Therefore, there are no pure dissolution-precipitation reactions possible during reactive melt transport with binary solid solution.

5.2.2. Riemann Problems Without Solution: Self-Limiting Reaction Fronts

It is possible to choose left and right states that cannot be connected by solution paths because the paths terminate at the solidus and the intermediate state lies in the solid region. For this case, a physically meaningful self-similar solution to the Riemann problem does not exist because it relies on the fact that a constant melt flux is maintained. Numerical simulations in section 5.4.3 show that these cases correspond to self-limiting reaction fronts where porosity and melt flux decay to zero. Although a self-similar solution does not exist in such cases, Figure 9 allows the identification of situations where reactive melt transport is self-limiting. An example of the graphical representation and identification of a self-limiting pathway is demonstrated in Figure 9. Left and right $\mathcal{CH}$ states are connected by pathways that intersect at an intermediate state that lies below the solidus. Therefore, the Riemann solution connecting the left state (symbolically denoted with a circle) and the right state (triangle) cannot reach their intermediate state (square), before porosity is forced to zero at the interface. Thus, flow is shut off and the reaction front is self-limiting.

5.3. Regime Diagram for Localization in Reactive Melt Transport

Although the localization of reactive melt transport into high-porosity channels is an intrinsically multidimensional phenomenon, its occurrence can be predicted from the porosity changes in one dimension. An upstream increase in porosity is a necessary condition for the localization of melt [*Chadam et al.*, 1986; *Szymczak and Ladd*, 2013]. This implies that the intermediate state must have a higher porosity than the right state. A strength of the analysis presented in section 4 is that it predicts the upstream porosity increases needed for localization. Figure 9 summarizes this analysis and allows the determination of porosity changes by inspection.

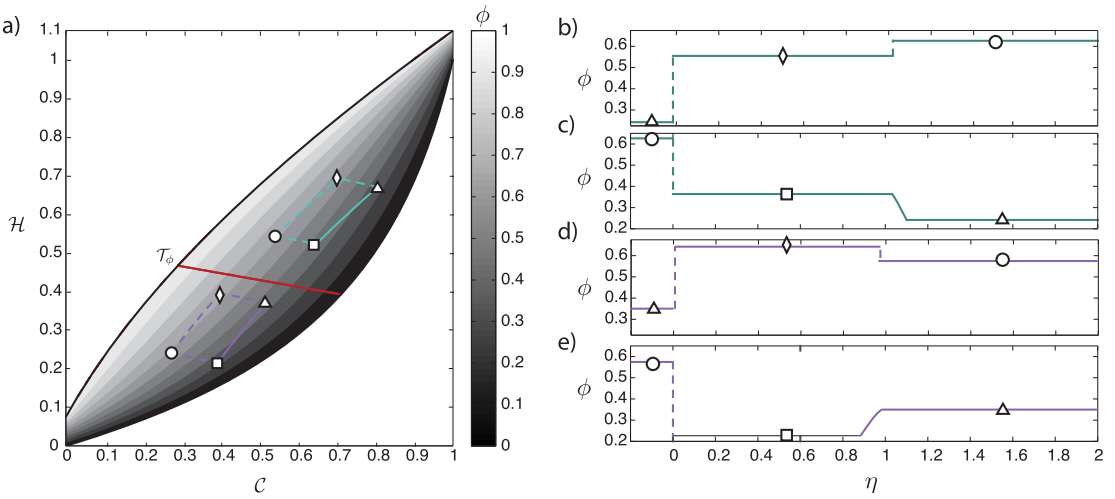

Figure 10. (a) The isotherm $\mathcal{T}_\phi$ lies along the locus where $\nabla\phi \cdot \mathrm{r}_2 = 0$. This splits the phase diagram into two distinct regimes. In the regime below $\mathcal{T}_\phi$, rarefactions are always stable and shocks are unstable. In the regime above $\mathcal{T}_\phi$, rarefactions may be unstable and shocks do not become unstable. (b–e) Since there are two distinct solution structures and two morphological regimes in phase space, four types of solution structure are possible. Figures 10b and 10c are associated with temperatures greater than $\mathcal{T}_\phi$ while Figures 10d and 10e are associated with temperatures less than $\mathcal{T}_\phi$.

Previous work on reaction-infiltration instabilities has only considered reaction fronts that are either sharp or of constant width due to the presence of dispersion and kinetics. Section 4 shows that reactive melt transport can lead to either sharp reaction fronts, shocks, or spreading reaction fronts, rarefactions. Since porosity can either increase or decrease across both reaction front morphologies, there are four distinct solution cases illustrated in Figure 10.

Inspection of Figure 9 shows that porosity initially increases along the fast path in the direction of the arrows before beginning to decrease roughly half way across the phase diagram. This is most pronounced near the solidus where the fast paths and porosity contours have opposite curvature. The locus of porosity maxima along the integral curves is given by

$$\nabla\phi \cdot \mathbf{r}_2 = 0, \tag{41}$$

and separates the phase diagram into two regions along an isotherm $\mathcal{T}_\phi$, as shown in Figure 10a. At $\mathcal{T}_\phi < \mathcal{T} < \mathcal{T}_r$, rarefaction fronts are associated with upstream increases in porosity and may be unstable while shocks are stable (in Figures 10b and 10c). At $\mathcal{T}_f < \mathcal{T} < \mathcal{T}_\phi$, shock reaction fronts induce an upstream increase in porosity and are unstable while rarefaction fronts induce an upstream decrease in porosity and are stable (in Figures 10d and 10e). To our knowledge, there is no detailed study of the reaction infiltration instability for reaction fronts that widen with time. Physical intuition suggests that instability depends on the relative growth rates of the instability and the widening of the front. In the problems considered here, the rarefaction fronts spread relatively slowly, (see Figure 6) and numerical solutions presented below suggest that rarefactions in regions of the phase diagram near the solidus are unstable as well.

5.4. Two-Dimensional Simulations of Melt Emanating From Fertile Heterogeneities

Fusible lithological heterogeneities that melt at lower temperatures are thought to play an important role during partial melting of the Earth's mantle [*Sobolev et al.*, 2007] and have been proposed to aid in the creation of high-porosity channels that allow the extraction of melt without reequilibration with the surrounding mantle [*Aharonov et al.*, 1995; *Spiegelman and Kelemen*, 2003; *Liang et al.*, 2010; *Hesse et al.*, 2011; *Weatherley and Katz*, 2012]. Despite the recognized importance of heterogeneities, most studies examine the localization of melt driven by a gradient reaction at the tectonic scale. Such models produce high-porosity channels with wavelengths on the order of a compaction length. In contrast, we examine the stability of a local reaction front emanating from the interface of a lithological heterogeneity and the ambient mantle on much smaller scales. The one-dimensional theory presented above predicts when the moving reaction front induces an upstream increase in porosity, a prerequisite for reaction infiltration instability.

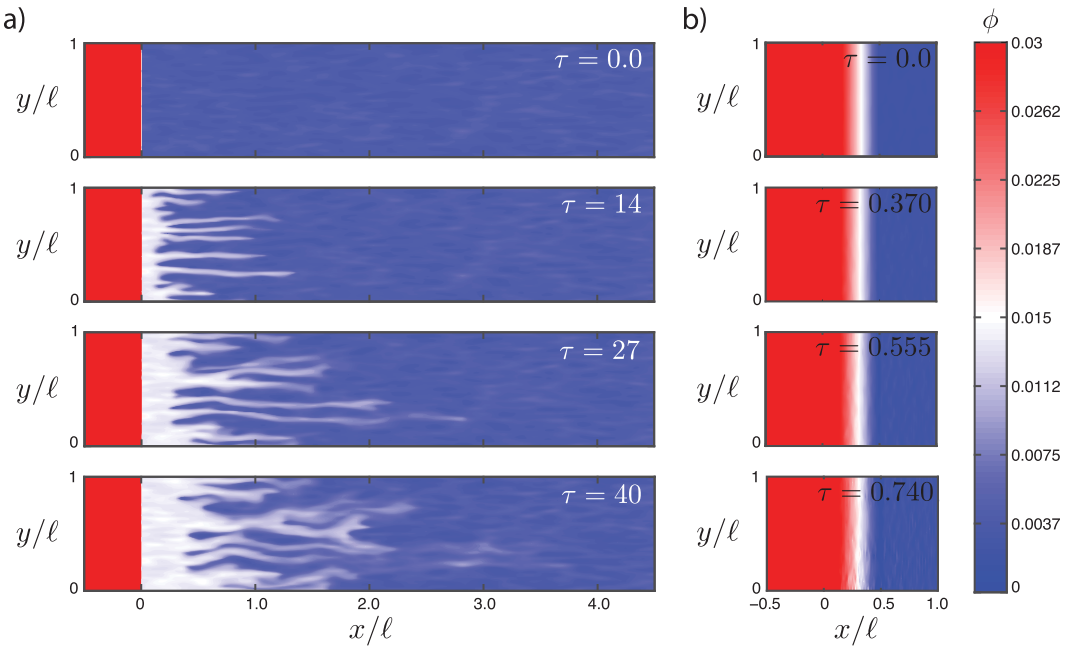

Figure 11. The evolution of the porosity field in numerical simulations of melt emanating from two different fertile heterogeneities with bulk compositions on either side of $\mathcal{T}_\phi$ in the regime diagram in Figure 10. In both simulations, melt flows from the left to the right. (a) The composition of the fertile heterogeneity on left and the composition of the ambient mantle on the right are given by $\mathcal{C}_l$=0.89 and $\mathcal{C}_r$=0.91. The initial enthalpy is constant across the domain and given by $\mathcal{H}_l$=$\mathcal{H}_r$=0.7125. The resultant initial porosities are ϕ_l=0.066 inside heterogeneity and ϕ_r=0.003 in the ambient mantle. (b) The composition of the fertile heterogeneity on left and the composition of the ambient mantle on the right are given by $\mathcal{C}_l$=0.307 and $\mathcal{C}_r$=0.333. The initial enthalpy is constant across the domain and given by $\mathcal{H}_l$=$\mathcal{H}_r$=0.125. The resultant initial porosities are ϕ_l=0.035 inside heterogeneity and ϕ_r=0.009 in the ambient mantle. For both simulations, $\mathrm{Pe}_\mathcal{C}$=10^6 and $\mathrm{Pe}_\mathcal{H}$=10^7, based on parameters given in Table 2. Note that the color scale has been truncated to emphasize the reacted zone.

5.4.1. Governing Equation for Melt Flow

Two-dimensional simulations have been performed to test if the magnitude of the porosity change is sufficient to induce reaction infiltration instability and localize melt transport. Similar to the one-dimensional analysis, it is assumed that the flow in the two-dimensional simulations is driven by a constant melt flux, q, across the left boundary.

In a viscously compacting medium, the overpressure, p=p_f −p_s, driving the melt flow is given by the following dimensionless Helmholtz equation,

$$-\nabla\cdot\left[\phi^3\nabla p\right]+\frac{\ell^2}{\delta^2}\phi p=0, \tag{42}$$

where ℓ is the dimension of the heterogeneity, δ is the compaction length, and the overpressure has been scaled by $q\mu\ell/K_0$ (see Appendix E for derivation). Previous work has considered heterogeneities with dimensions that are comparable or even larger than the compaction length [*Weatherley and Katz*, 2012]. Here we consider reaction infiltration instabilities occurring at spatial scales much smaller than the compaction length. To resolve such small length scales, the domain width in the simulations presented below has been chosen as $\ell = 0.2\delta$. In the limit of $\ell^2/\delta^2 \ll 1$, the Helmholtz equation reduces to the Poisson equation governing fluid flow in rigid porous media. At scales of interest here, ℓ^2/δ^2=0.04. Therefore, the porous medium is approximately rigid and the simplified governing equation for the pressure is solved.

5.4.2. Fertile Heterogeneities That Lead to Reactive Infiltration Instability

Instantaneous decompression melting of a fusible heterogeneity leads to a Riemann-type initial condition with an initial step in bulk composition and a constant enthalpy throughout the domain. We first consider this problem to test the predictions of the one-dimensional theory before considering a more realistic initial condition below.

Figure 11a shows the evolution of the porosity due to melt emanating from a fertile heterogeneity after instantaneous decompression melting. For this simulation, the initial enthalpy is constant and the bulk

Table 2. Dimensional Parameters Used for Two-Dimensional Model Calculations Shown in Figure 12

Symbol	Meaning	Value
K_0	Reference permeability	1×10^{-14} m^2
μ	Viscosity of melt	1 Pa s
η_0	Reference shear viscosity of solid	1×10^{19} 1 Pa s
k_m	Thermal conductivity of melt	1×10^{-5} m/s^2
k_s	Thermal conductivity of solid	1×10^{-6} m/s^2
ϑ	Tortuosity	$\sqrt{2}$
D	Hydrodynamic dispersion	1×10^{-7} m^2/s
δ	Compaction length	100 m
ℓ	Dimension of heterogeneity	20 m

compositions of both the heterogeneity and the ambient mantle are such that they plot on the refractory side of $\mathcal{T}_\phi$ in the regime diagram shown in Figure 10a. This initial condition yields a reacted zone with a porosity higher than the ambient mantle, similar to the one-dimensional profile shown in Figure 10c, with the structure

$$\mathbf{u}_I \xrightarrow{\mathscr{C}_1} \mathbf{u}_i \xrightarrow{\mathscr{R}_2} \mathbf{u}_r.$$

The simulation assumes instantaneous decompression melting of the heterogeneity, which leads to an initial condition with constant enthalpy throughout the domain, but an increased porosity inside the heterogeneity. Although, the propagating reaction front is a rarefaction and thus slowly spreads with time, localization of the flow is observed. This suggests that the perturbations grow faster than the reaction front, $\mathscr{R}_2$, widens with time. Figure 11a shows the formation of high-porosity channels due to a reaction infiltration instability emanating from the interface between a fertile partially molten heterogeneity and the low-porosity, ambient mantle.

The porosity of the reacted zone is substantially lower than within the heterogeneity because the enthalpy of the fertile melt is not sufficient to further raise the porosity of the refractory ambient mantle. Nonetheless, the upstream porosity increase in Figure 11a is more than eightfold and sufficient to localize melt into higher-porosity channels. For the Péclet numbers chosen here (Table 2), the wavelength of the channels is approximately $\delta/25$.

It is important to note that the speed of the advancing reaction front is very slow relative to percolating melt as shown by Figure 5b. This is expected because the end-members in an ideal solid solution are highly compatible and at low porosities there is an abundance of solid available for reaction with the melt. Reaction fronts may propagate significantly faster in reactive melt transport models that consider multiple solid phases, if the volume fractions of the reactive solid phases are small and the solubilities in the melt are high [*Liang et al*., 2010].

5.4.3. Fertile Heterogeneities That Lead to Self-Limiting Flow

Figure 11b also shows the evolution of the porosity due to melt emanating from a fertile heterogeneity after instantaneous decompression melting at constant initial enthalpy. This case was chosen to have the same initial porosity within the fertile heterogeneity and ambient mantle as in Figure 11a. However, in this case, the $\mathcal{CH}$ states of both the heterogeneity and ambient mantle plot on the fusible side of $\mathcal{T}_\phi$ in the regime diagram in Figure 10a.

This initial condition corresponds to a Riemann problem without a solution, as discussed in section 5.2.2 and illustrated by the unphysical intermediate state below the solidus plotted as a square in Figure 9. To further illustrate the self-limiting nature of reactive transport, the numerical simulation in Figure 11b is initialized with a continuous transition zone rather than a sharp boundary between the interior of the fertile heterogeneity and the ambient mantle. This allows the porosity in the reacted zone to gradually approach zero, at which point melt flux stops. The formation of a zero porosity shell around the heterogeneity stops the leakage of melt from entering the mantle.

If partial melting is modeled using a binary solid solution liquid solution, the behavior of a fertile heterogeneity depends on its absolute concentration, in addition to compositional differences between itself and the refractory background. This dependence of the behavior on absolute concentration has not been appreciated previously. The regime diagram presented in Figure 10a can be used to select compositions for fertile heterogeneities conducive to reactive infiltration instability and channelization.

5.4.4. Melt Emanating From a Fertile Heterogeneity With a Diffusive Halo

The examples shown in Figure 11 assume that melting is instantaneous and that melt migration commences immediately. If time elapses between the onset of melting and the beginning of melt migration, heat conduction acts to bring the heterogeneity into thermal equilibrium with the surrounding mantle. Given that the latent heat of fusion has lowered the temperature within the fertile heterogeneity, heat is

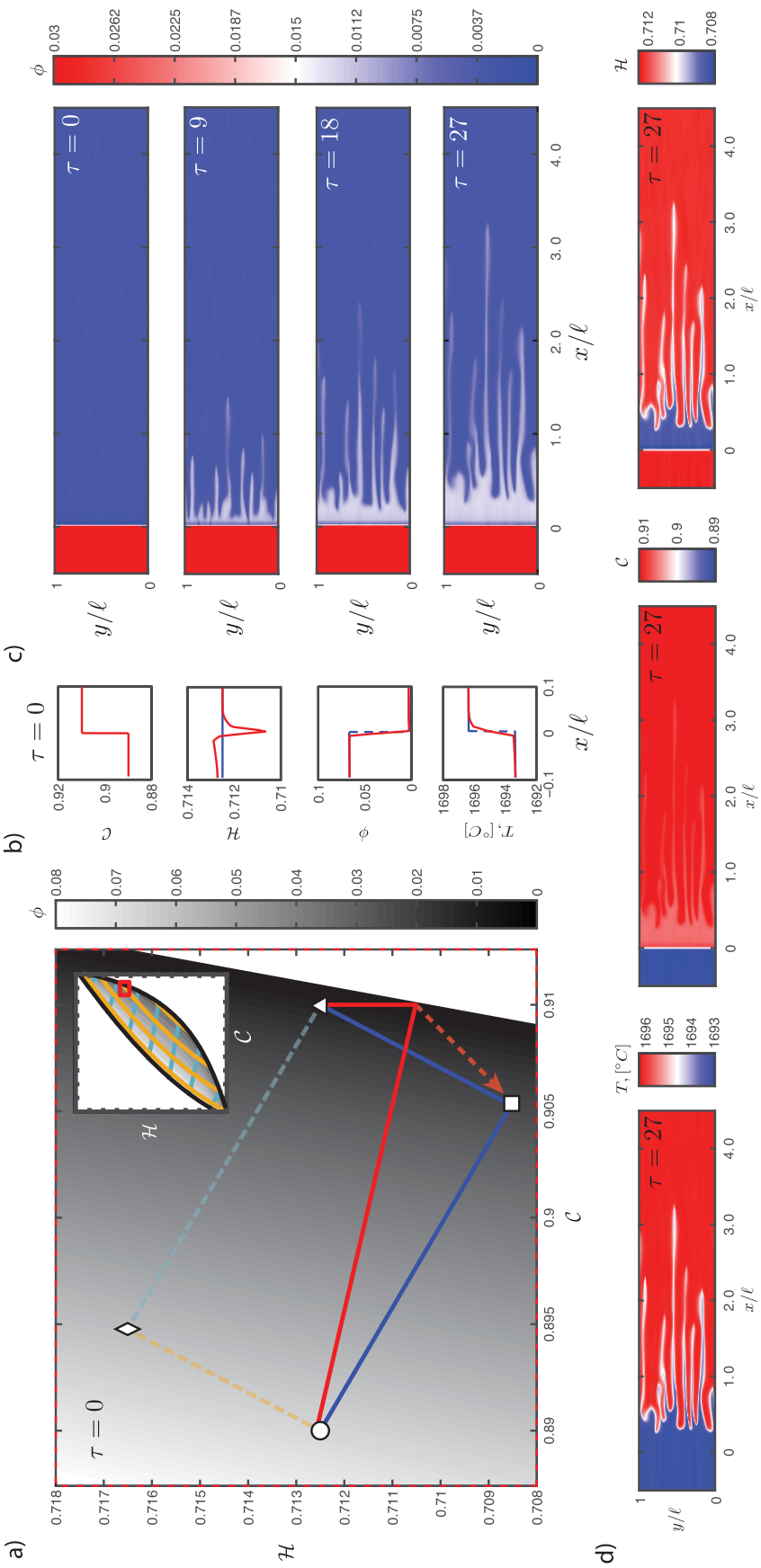

Figure 12. The evolution of the porosity field in numerical simulations of melt emanating from a fertile heterogeneity with a thermal halo. (a) The conductive initial condition (red) and the solution path predicted by the one-dimensional analysis of the corresponding Riemann problem (blue) in $\mathcal{CH}$ phase space. The arrow indicates the evolution of the solution path. Inlay shows the location of the plot in Figure 9. (b) The conductive initial condition (red) in comparison with the initial condition of the corresponding Riemann problem shown in Figure 11a. (c) Evolution of the porosity field. (d) The temperature, T, bulk composition, $\mathcal{C}$, and bulk enthalpy, $\mathcal{H}$, fields at the end of the simulation. Dimensional values are computed from the parameters given in Tables 1 and 2.

conducted from the ambient mantle into the cooler heterogeneity. This leads to the smoothing of the thermal gradient in the immediate vicinity of the heterogeneity and creates a halo in the ambient mantle where the temperature, enthalpy, and porosity are reduced [*Katz and Rudge*, 2011; *Weatherley and Katz*, 2012].

To test if the reactive infiltration instability still occurs in the presence of such a thermal halo, a reactive melt transport simulation was conducted that used a one-dimensional conductive profile as an initial condition. This conductive profile was created by allowing the initial condition for the Riemann problem in Figure 11a to evolve until porosity in the thermal halo was reduced to 0.0001. Figures 12a and 12b compare the Riemann and the conductive initial condition. Note that conduction has slightly shifted the location of the fertile heterogeneity, corresponding to the circle plotted in $\mathcal{CH}$ phase space. As the reactive melt transport proceeds, the solution path in $\mathcal{CH}$ phase space evolves back toward the path predicted by the one-dimensional analysis, as indicated by the arrow in Figure 12a.

The evolution of the porosity field due to melt emanating from a fertile heterogeneity with a thermal halo is shown in Figure 12c. A reactive infiltration instability similar to Figure 11a is observed. The porosity minimum in the thermal halo accelerates the melt flow and increases the effective Péclet number in the halo. As expected, this decreases the width of the reaction front and therefore the wavelength of the instability.

Figure 12d illustrates temperature, composition, and enthalpy fields corresponding to the last porosity field in Figure 12c. The temperature has been redimensionalized and shows that melting in the fertile heterogeneity drops the temperature by approximately 4°. As this cooled melt emanates from the fertile heterogeneity, the mantle is refertilized as the fusible component partitions from the melt into the solid.

As long as thermal conduction does not reduce the porosity to zero, preventing any flow, the long-term behavior of the moving reaction front converges to the one-dimensional analysis. This is due to the self-similar nature of reactive transport, where perturbations of the initial condition do not affect the long-term behavior advancing front.

In previous work on channel formation during melt extraction beneath mid-ocean ridges, the channels often nucleate shallow and grow downward into the mantle. In this context, the fertile heterogeneity provides the increased melt flux required to initiate channel formation [*Weatherley and Katz*, 2012; *Hewitt*, 2010]. In contrast, here we suggest that the high-porosity channels may nucleate at the heterogeneity itself. While the channels formed by a frontal reaction infiltration instability considered here are small, they may provide the necessary perturbation required to induce channeling over larger distance driven by the large-scale gradient reaction induced by orthopyroxene dissolution [*Liang et al*., 2011].

6. Conclusions

This manuscript shows that the theory of hyperbolic conservation laws provides a general framework for reactive melt transport in the limit of local thermodynamic equilibrium and negligible hydrodynamic dispersion. The framework is illustrated with a detailed study of a simplified, ideal binary solid solution liquid solution modeled after the olivine phase diagram. The analysis yields a grid of all possible solution paths contained within a modified phase diagram in composition-enthalpy space. These pathways show that dissolution-precipitation and melting-freezing are tightly coupled in solid solutions and pure melting is only possible at end-members. For the binary solid solution considered here, reactive melt transport across an initial lithological boundary leads to the formation of a reacted zone that is bounded between a stationary and an advancing reaction front. Unlike systems with pure solid phases which always lead to sharp fronts, the solid solution considered here can also give rise to spreading fronts. The stability of the advancing reaction front depends on the porosity of the reacted zone, which can be determined by inspection of the modified phase diagram presented in this manuscript.

The analysis predicts the instability of the reaction front that forms in numerical simulations of melt emanating from a fusible heterogeneity into the ambient mantle. Furthermore, the numerical simulation highlights the ability of heterogeneities to seed high-porosity channels at wavelengths much smaller than a compaction length. The analysis also shows that the behavior of a fertile heterogeneity depends on its absolute concentration, in addition to compositional differences between itself and the refractory background. The

analysis allows the construction of a regime diagram that predicts if melt emanating from a fertile heterogeneity localizes into high-porosity channels or develops a zero porosity shell. This illustrates the complexities of reactive melt transport, despite the simplicity of the underlying phase behavior.

Appendix A: Gibbs Free Energy for Binary Solid Solution With Liquid Solution

The description of Gibbs free energy begins with equilibrium expressions for end-members of a solid solution in terms of the Gibbs energies of fusion. If the solid solution is ideal, $\Delta H = 0$ and end-member activities are equal to their respective mole fractions. The change in Gibbs free energy is given as,

$$\Delta G_i^0 = RT \ln\left(\frac{X_{i,s}}{X_{i,m}}\right). \tag{A1}$$

The full temperature dependence of ΔG_i^0 is,

$$\Delta G_i^0 = \Delta H_i^0 - T\Delta S_i^0, \tag{A2}$$

where the enthalpy and entropy for end-member i at the end-member melting temperature $(T_m,\ i)$ are,

$$\Delta H_i^0 = \Delta H_i^{T_{melt}} + \int_{T_{melt}}^{T} (c_{p\,m,i} - c_{p\,s,i})\mathrm{d}T = \Delta H_i^{T_{melt}} + \Delta c_{p\,i}(T - T_{melt}), \tag{A3}$$

$$\Delta S_i^0 = \Delta S_i^{T_{melt}} + \int_{T_{melt}}^{T} \frac{\Delta c_{p\,i}}{T}\mathrm{d}T = \Delta S_i^{T_{melt}} + \Delta c_{p\,i} \ln\left(\frac{T}{T_{melt}}\right), \tag{A4}$$

$$\Delta G_i^0 = \Delta H_i^{T_{melt}} + \int_{T}^{T_{melt}} \Delta c_{p\,i}\mathrm{d}T - T\left(\Delta S_i^{T_{melt}} + T\int_{T}^{T_{melt}} \frac{\Delta c_{p\,i}}{T}\mathrm{d}T\right), \tag{A5}$$

where subscript m denotes the temperature of melting/freezing point and $\Delta c_{p\,i} = (c_{p\,s,i} - c_{p\,m,i})$ is the difference melt-solid specific heat over the temperature range spanned by the liquidus curve for each end-member, respectively.

Assuming local thermodynamic equilibrium, at the melting point of either end-member, the Gibbs equation becomes,

$$\Delta G_i^0 = \Delta H_i^{T_{melt}} - T_{melt}\Delta S_i^{T_{melt}} = 0, \tag{A6}$$

which implies that,

$$\Delta S_i^{T_{melt}} = \frac{\Delta H_i^{T_{melt}}}{T_{melt}}. \tag{A7}$$

Substitution of expressions for enthalpy and entropy into the Gibbs energy of fusion equation for both end-members yields

$$\Delta G_i^0 = \Delta H_i^{T_{melt}}\left(\frac{T_{melt} - T}{T_{melt}}\right) + \Delta c_{p\,i}\left(\frac{\left[\left(1 - \ln\left(\frac{T}{T_{melt}}\right)\right)T - T_{melt}\right]}{T_{melt}}\right). \tag{A8}$$

For a binary solid solution with a fusible and refractory end-member, $i = f$ or $i = r$. Given known melting temperatures for each end-member, $T_m = T_f$ or $T_m = T_r$, and known $\Delta c_{p\,i}$ at both end-members, the Gibbs free energy of both end-members can be calculated.

The final term multiplied by $\Delta c_{p\,i}$ can be neglected because the enthalpy and entropy of fusion at the melting point are very large relative to the corrections introduced by the specific heat terms. Thus, a simplified version of the Gibbs energy of fusion for derivation of the phase diagram can be written as,

$$\Delta G_i^0 = \Delta H_i^{T_{melt}}\left(\frac{T_{melt} - T}{T_{melt}}\right). \tag{A9}$$

Throughout the main body of the text, the superscript for the change in Gibbs free energy is dropped. The change in free energy for the refractory end-member is given by ΔG_r and the fusible end-member as ΔG_f.

Appendix B: Enthalpy in Binary Solid-Solution Liquid-Solution

B1. Full System

Assuming negligible pressure changes, the specific enthalpies of end-members of the solid-solution are given by

$$h_{s,f} = h^0_{s,f} + c_{p,sf}(T - T_0), \tag{B1}$$

$$h_{s,r} = h^0_{s,r} + c_{p,sr}(T - T_0), \tag{B2}$$

where the parameters $c_{p,sf}$ and $c_{p,sr}$ are the specific heat capacities at constant pressure for the fusible and refractory end-members. Their reference enthalpies, $h^0_{s,f}$ and $h^0_{s,r}$, are given at 298°K, T_0. Finally, the specific latent heats of the two end-members are given by

$$\Delta H_r = \Delta H_r^{T_r} - \Delta c_{p,r}(T - T_r), \tag{B3}$$

$$\Delta H_f = \Delta H_f^{T_f} - \Delta c_{p,f}(T - T_f), \tag{B4}$$

where $\Delta c_{p,r} = c_{p,mr} - c_{p,sr}$ and $\Delta c_{p,f} = c_{p,mf} - c_{p,sf}$ are the differences in specific heat capacity between the liquid and solid phases of the end-members. Their reference enthalpies of fusion, $\Delta H_r^{T_r}$ and $\Delta H_f^{T_f}$, are given at their respective melting points.

B2. Enthalpy of Solid Solution

The enthalpy solid solution is the composition-weighted average of the temperature adjusted solid end-member enthalpies:

$$h_s(X_{r,s}(T), T) = h_{s,r}(X_{s,r}(T)) + h_{s,f}(1 - X_{s,r}(T)). \tag{B5}$$

We assume that specific heats (at $dP \approx 0$) are constant but not necessarily equal across end-members and phases. The parameters $c_{p,sf}$ and $c_{p,sr}$ are the solid specific heat constants for the fusible and refractory end-members. Solid enthalpy expressions become,

$$h_{s,f} = h^0_{s,f} + c_{p,sf}(T - T_0), \tag{B6}$$

$$h_{s,r} = h^0_{s,r} + c_{p,sr}(T - T_0), \tag{B7}$$

and can be substituted into (B5) to obtain the $h_s(T)$ for the enthalpy of solid-solution.

B3. Enthalpy of Molten Solution

At equilibrium when both the solid and melt phases present, the enthalpy of the liquid phase is that of the solid phase plus the contribution of latent heat from the phase change. The molar enthalpy of the liquid can be described as,

$$h_m(X_r, T) = h_s(T) + \Delta H(X_r, T). \tag{B8}$$

where ΔH the latent heat of fusion adjusted for a linear mixture of end-members across the phase diagram and X_r is the bulk mole fraction of the binary system in terms of the refractory end-member. The enthalpy of fusion is a function of the overall composition of the system due to differences in the latent heats and heat capacities of the end-members. The terms $\Delta H_r^{T_r}$ and $\Delta H_f^{T_f}$ in (B6) and (B7) represent the molar latent heat of fusion at each end-member at their respective melting temperatures. The latent heat of fusion in (B8) is presented as the mole fraction weighted average of ΔH for the refractory and fusible end-members across the solid-solution:

$$\Delta H = X_r \Delta H_r(T) + (1 - X_r)\Delta H_f(T). \tag{B9}$$

The full dimensional expression for enthalpy for a specific porosity, ϕ, can now be written as a function of X_r and T given the phase densities, ρ_i, the specific heats for liquid and solids at both end-members, and their reference enthalpies of fusion:

$$H = \rho_l \phi \left(h_{s,r}(X_{s,r}) + h_{s,f}(1 - X_{s,r}) + \Delta H\right) + \rho_s(1 - \phi)\left(h_{s,r}(X_{s,r}) + h_{s,f}(1 - X_{s,r})\right). \tag{B10}$$

The densities of both phases, ρ_m and ρ_s, are written as a function of X_r and the molar volumes, $V_{p,i}$, of both phases at end-members,

$$\rho_m = \frac{1}{V_{l,r}X_{m,r} + V_{l,f}(1-X_{m,r})}, \tag{B11}$$

$$\rho_s = \frac{1}{V_{s,r}X_{s,r} + V_{s,f}(1-X_{s,r})}. \tag{B12}$$

B4. Simplified System

In the simplified system, $h^0_{sf} = h^0_{sr} = h_0$ and $c_{p,sf} = c_{p,sr} = c_p$ so that the specific enthalpy of the two end-members are the same the specific enthalpy of the solid is given by

$$h_s = h_0 + c_p(T - T_0). \tag{B13}$$

If the system is simplified further such that $\rho_m = \rho_s$, the latent heat of fusion can be described by the constant $\Delta H = L$. The thermodynamic properties needed to solve the simplified system are given in the main text by Table 1.

Appendix C: Dimensionless Equations for Simplified One-Dimensional Model Equations

The dimensionless variables described in section 3,

$$\mathcal{C} = \frac{C}{\rho}, \quad \mathcal{T} = \frac{T - T_f}{T_r - T_f}, \quad \zeta = \frac{x}{\ell}, \quad \text{and} \quad \tau = \frac{tq}{\ell}, \tag{C1}$$

are inserted into the nonlinear algebraic system of equations governing the transport of conservation and enthalpy:

$$\mathcal{C} = \phi X_{m,r} + (1-\phi)X_{s,r}, \tag{C2}$$

$$\mathcal{H} = \frac{\phi}{\mathrm{Ste}} + \mathcal{T}, \tag{C3}$$

$$X_{m,r}(\mathcal{T}) = \left[\frac{1 - e^{(\Theta_1(1-\mathcal{T})/(\Theta_3+\mathcal{T}))}}{e^{(-\Theta_2\mathcal{T}/(\Theta_3+\mathcal{T})} - e^{(\Theta_1(1-\mathcal{T})/(\Theta_3+\mathcal{T}))}}\right], \tag{C4}$$

$$X_{s,r}(\mathcal{T}) = \left[\frac{\left[1 - e^{(\Theta_1(1-\mathcal{T})/(\Theta_3+\mathcal{T}))}\right] e^{(-\Theta_2\mathcal{T}/(\Theta_3+\mathcal{T})}}{e^{(-\Theta_2\mathcal{T}/(\Theta_3+\mathcal{T})} - e^{(\Theta_1(1-\mathcal{T})/(\Theta_3+\mathcal{T}))}}\right]. \tag{C5}$$

The dimensionless parameters set by end-member melting temperatures and the constant latent heat of fusion are

$$\Theta_1 = \frac{L}{RT_r}, \quad \Theta_2 = \frac{L}{RT_f}, \quad \Theta_3 = \frac{T_f}{\Delta T}. \tag{C6}$$

The parameters Θ_1 and Θ_2 are ratios of molar energy released in terms of the end-member melting temperatures. Adjustment of these parameters controls the curvature of the phase diagram. The ratio Θ_3 weighs the melting temperature of the first incremental bit of melt possible in the two-phase region of phase space against the entire temperature range where the end-members can coexist in two-phase equilibrium.

The dimensionless expression for enthalpy is set by substituting $\mathcal{T}$ into the dimensional expressions for the enthalpy liquidus and solidus h_m and h_s. The expressions for dimensionless enthalpy follow as,

$$\mathcal{H}_s = \frac{h_s - h_s^{T_f}}{c_p \Delta T} = \mathcal{T}, \tag{C7}$$

$$\mathcal{H}_m = \frac{h_m - h_s^{T_f}}{c_p \Delta T} = \mathcal{T} + \frac{L}{c_p \Delta T}. \tag{C8}$$

Using equations (C7) and (C8), the full dimensionless enthalpy budget (C3) is constructed.

Appendix D: Flux Gradient for Melt Transport Across a Discontinuity: Simplified Model Equations

D1. Flux Derivatives

The entries for the flux gradient are,

$$f_{\mathcal{C},\mathcal{C}} = \frac{\mathrm{d}X_m}{\mathrm{d}\mathcal{T}}\frac{\partial \mathcal{T}}{\partial \mathcal{C}}, \tag{D1}$$

$$f_{\mathcal{C},\mathcal{H}} = \frac{\mathrm{d}X_m}{\mathrm{d}\mathcal{T}}\frac{\partial \mathcal{T}}{\partial \mathcal{H}}, \tag{D2}$$

$$f_{\mathcal{H},\mathcal{C}} = \frac{\mathrm{d}h_m}{\mathrm{d}\mathcal{T}}\frac{\partial \mathcal{T}}{\partial \mathcal{C}}, \tag{D3}$$

$$f_{\mathcal{H},\mathcal{H}} = \frac{\mathrm{d}h_m}{\mathrm{d}\mathcal{T}}\frac{\partial \mathcal{T}}{\partial \mathcal{H}}. \tag{D4}$$

Within the two-phase region, these derivatives must be evaluated through implicitly differentiating the function $\not\Delta(\mathcal{C},\mathcal{H},\mathcal{T})$ along with differentiating equations (C4) and (C8) with respect to dimensionless temperature.

The derivative with respect to dimensionless temperature needed from the function $X_{m,r}$ is as follows:

$$\frac{\mathrm{d}X_m}{\mathrm{d}\mathcal{T}} = \frac{\clubsuit\heartsuit}{\spadesuit-\clubsuit} + \frac{((1-\clubsuit)\spadesuit\diamondsuit-\clubsuit\heartsuit)}{(\spadesuit-\clubsuit)^2}, \tag{D5}$$

where,

$$\clubsuit = e^{\Theta_1(1-\mathcal{T})/(\Theta_3+\mathcal{T}))}, \tag{D6}$$

$$\spadesuit = e^{-\Theta_2\mathcal{T}/(\Theta_3+\mathcal{T})}, \tag{D7}$$

$$\heartsuit = -\frac{\Theta_1}{(\Theta_3+\mathcal{T})} - \frac{\Theta_1(1-\mathcal{T}))}{(\Theta_3+\mathcal{T})^2}, \tag{D8}$$

$$\diamondsuit = \frac{\Theta_2\mathcal{T}}{(\Theta_3+\mathcal{T})^2} - \frac{\Theta_2}{(\Theta_3+\mathcal{T})}, \tag{D9}$$

$$\triangle = e^{\Theta_1(1-\mathcal{T})/(\Theta_3+\mathcal{T}))-\Theta_2\mathcal{T}/(\Theta_3+\mathcal{T})}. \tag{D10}$$

The derivative with respect to dimensionless temperature needed from the function X_s is,

$$\frac{\mathrm{d}X_s}{\mathrm{d}\mathcal{T}} = \frac{\heartsuit\triangle-(1-\clubsuit)\spadesuit\diamondsuit}{\spadesuit-\clubsuit} + \frac{(1-\clubsuit)\spadesuit(\diamondsuit\spadesuit-\clubsuit\heartsuit)}{(\spadesuit-\clubsuit)^2}. \tag{D11}$$

Mercifully, the derivative with respect to dimensionless temperature needed from the function $\not h_m$ is

$$\frac{\mathrm{d}\not h_m}{\mathrm{d}\mathcal{T}} = 1. \tag{D12}$$

For the partial derivatives in the flux function, $\frac{\partial \mathcal{T}}{\partial \mathcal{C}}$ and $\frac{\partial \mathcal{T}}{\partial \mathcal{H}}$ are found via implicit differentiation:

$$\frac{\partial \mathcal{T}}{\partial \mathcal{C}} = \frac{-\frac{\partial \not\Delta}{\partial \mathcal{C}}}{\not\Delta}, \tag{D13}$$

$$\frac{\partial \mathcal{T}}{\partial \mathcal{H}} = \frac{-\frac{\partial \mathcal{C}}{\partial \mathcal{H}}}{\mathcal{D}}, \tag{D14}$$

where the denominator, which is denoted after the Egyptian hieroglyph for "D"

$$\mathcal{D} = \frac{\partial \mathcal{C}}{\partial \mathcal{T}} + \frac{\partial \mathcal{C}}{\partial X_m}\frac{\mathrm{d}X_m}{\mathrm{d}\mathcal{T}} + \frac{\partial \mathcal{C}}{\partial X_s}\frac{\mathrm{d}X_s}{\mathrm{d}\mathcal{T}}. \tag{D15}$$

The partial derivatives needed to construct the flux function from the implicit function are,

$$\frac{\partial \mathcal{C}}{\partial \mathcal{C}} = 1, \tag{D16}$$

$$\frac{\partial \mathcal{C}}{\partial \mathcal{H}} = \mathrm{Ste}(X_s - X_m), \tag{D17}$$

$$\frac{\partial \mathcal{C}}{\partial \mathcal{T}} = \mathrm{Ste}(X_m - X_s), \tag{D18}$$

$$\frac{\partial \mathcal{C}}{\partial X_s} = \mathrm{Ste}(\mathcal{H} - \mathcal{T}) - 1, \tag{D19}$$

$$\frac{\partial \mathcal{C}}{\partial X_m} = -\mathrm{Ste}(\mathcal{H} - \mathcal{T}). \tag{D20}$$

Appendix E: Compaction

The governing equations for melt transport are obtained from the continuity equation of the two-phase mixture,

$$\nabla \cdot (\phi \mathbf{v}_m + (1-\phi)\mathbf{v}_s) = 0, \tag{E1}$$

where $\mathbf{v}_m$ and $\mathbf{v}_s$ are the velocities of melt and solid phases. The volumetric flux of the melt in the reference frame of the solid is given by,

$$\mathbf{q} = \phi(\mathbf{v}_m - \mathbf{v}_s) = -\frac{K}{\mu}(\nabla p - \Delta\rho g \hat{z}), \tag{E2}$$

where g is gravitational acceleration, $\hat{z}$ denotes upward unit vector, $K = K_0\phi^3$ is the permeability of the porous medium, μ is the melt viscosity, and $\Delta\rho$ is the density difference between the liquid and solid phases. In a viscously compacting medium, the melt flow is driven by overpressure, defined as

$$p = p_m - p_s = \xi \nabla \cdot \mathbf{v}_s, \tag{E3}$$

where p_m and p_s are the pressure of the melt and solid phases and $\xi = \eta_0/\phi + 4/3\,\eta_0 \approx \eta_0/\phi$, where η_0 is the reference shear viscosity. Substituting (E1) and (E2) into (E3), we obtain a governing equation for the evolution of the fluid overpressure,

$$-\nabla \cdot \left[\frac{K}{\mu}\nabla p\right] + \frac{p}{\xi} = -\frac{\Delta\rho g}{\mu}\left(\frac{\mathrm{d}K}{\mathrm{d}z}\right). \tag{E4}$$

Scaling distance by the dimension, ℓ, of the heterogeneity and scaling the pressure with $q\mu\ell/K_0$ the dimensionless Helmholtz equation is given by,

$$-\nabla \cdot [\phi^3 \nabla p] + \frac{\ell^2}{\delta^2}\phi p = -\frac{\Delta\rho g \mu}{q K_0}\left(\frac{\mathrm{d}\phi^3}{\mathrm{d}z}\right), \tag{E5}$$

where the compaction length, $\delta = \sqrt{K_0\eta_0/\mu}$. In the simulations presented here, the domain is horizontal

and flows are driven by a flux, q, across the left boundary rather than density differences. Therefore, the right-hand side of (E5) is zero.

Acknowledgments
This material is based upon work supported by the National Science Foundation under grant EAR-CMG-1025321. The authors would also like to acknowledge helpful discussions with Mark Ghiorso and William Carlson and the constructive reviews of Tobias Keller and an anonymous reviewer.

References

Aharonov, E., J. A. Whitehead, P. B. Kelemen, and M. Spiegelman (1995), Channeling instability of upwelling melt in the mantle, *J. Geophys. Res.*, *100*, 20,433–20,450, doi:10.1029/95JB01307.

Appelo, C., and D. Postma (2010), Flow and transport, in *Geochemistry, Groundwater and Pollution*, 2nd ed., CRC Press, A.A. Balkema Publishers, Leiden.

Bryant, S., R. Schechter, and L. Lake (1987), Mineral sequences in precipitation/dissolution waves, *AIChE J.*, *33*(8), 1271–1287.

Chadam, J., D. Hoff, E. Merino, P. Ortoleva, and A. Sen (1986), Reactive infiltration instabilities, *IMA J. Appl. Math.*, *36*(3), 207–221, doi:10.1093/imamat/36.3.207.

DePaolo, D. J. (1996), High-frequency isotopic variations in the Mauna Kea tholeiitic basalt sequence: Melt zone dispersivity and chromatography, *J. Geophys. Res.*, *101*, 11,855–11,864, doi:10.1029/95JB03494.

DeVault, D. (1943), The theory of chromatography, *J. Am. Chem. Soc.*, *65*(4), 532–540, doi:10.1021/ja01244a011.

Glueckauf, E. (1945), Chromatography of two solutes, *Nature*, *156*(3935), 205–206, doi:10.1038/155401a0.

Godard, M., J.-L. Bodinier, and G. Vasseur (1995), Effects of mineralogical reactions on trace element redistributions in mantle rocks during percolation processes: A chromatographic approach, *Earth Planet. Sci. Lett.*, *133*, 449–461.

Hauri, E. H. (1997), Melt migration and mantle chromatography, 1: Simplified theory and conditions for chemical and isotopic decoupling, *Earth Planet. Sci. Lett.*, *153*, 1–19.

Hauri, E. H., and M. D. Kurz (1997), Melt migration and mantle chromatography, 2: A time-series Os isotope study of Mauna Loa volcano, Hawaii, *Earth Planet. Sci. Lett.*, *153*, 21–36, doi:10.1016/S0012-821X(97)00158-1.

Hesse, M. A., A. R. Schiemenz, Y. Liang, and E. M. Parmentier (2011), Compaction-dissolution waves in an upwelling mantle column, *Geophys. J. Int.*, *187*(3), 1057–1075, doi:10.1111/j.1365-246X.2011.05177.x.

Hewitt, I. J. (2010), Modelling melting rates in upwelling mantle, *Earth Planet. Sci. Lett.*, *300*, 264–274, doi:10.1016/j.epsl.2010.10.010.

Hinch, E. J., and B. S. Bhatt (1990), Stability of an acid front moving through porous rock, *J. Fluid Mech.*, *212*, 279–288, doi:10.1017/S0022112090001963.

Hofmann, A. (1972), Chromatographic theory of infiltration metasomatism and its application to feldspars, *Am. J. Sci.*, *272*, 69–90.

Katz, R. F. (2008), Magma dynamics with the enthalpy method: Benchmark solutions and magmatic focusing at mid-ocean ridges, *J. Petrol.*, *49*(12), 2099–2121, doi:10.1093/petrology/egn058.

Katz, R. F., and J. F. Rudge (2011), The energetics of melting fertile heterogeneities within the depleted mantle, *Geochem. Geophys. Geosyst.*, *12*, Q0AC16, doi:10.1029/2011GC003834.

Katz, R. F., M. Spiegelman, and B. Holtzman (2006), The dynamics of melt and shear localization in partially molten aggregates, *Nature*, *442*(7103), 676–679, doi:10.1038/nature05039.

Kelemen, P. B., N. Shimizu, V. Salters, and J. M. (1995), Extraction of mid-ocean-ridge basalt from the upwelling mantle by focused flow of melt in dunite channels, *Nature*, *375*, 747–753, doi:10.1038/375747a0.

Kelemen, P. B., G. Hirth, N. Shimizu, M. Spiegelman, and H. J. Dick (1997), A review of melt migration processes in the adiabatically upwelling mantle beneath oceanic spreading ridges, *Philos. Trans. R. Soc. London A*, *355*, 283–318, doi:10.1098/rsta.1997.0010.

Keller, T., D. A. May, and B. J. P. Kaus (2013), Numerical modelling of magma dynamics coupled to tectonic deformation of lithosphere and crust, *Geophys. J. Int.*, *195*(3), 1406–1442, doi:10.1093/gji/ggt306.

Korzhinskii, D. S. (1965), The theory of systems with perfectly mobile components and processes of mineral formation, *Am. J. Sci.*, *263*, 193–205.

Korzhinskii, D. S. (1968), The theory of metasomatic zoning, *Miner. Deposita*, *3*, 222–231, doi:10.1007/BF00207435.

Lax, P. D. (1973), *Hyperbolic Systems of Conservation Laws and the Mathematical Theory of Shock Waves*, Soc. for Ind. and Appl. Math., Philadelphia.

LeVeque, R. J. (1991), Numerical methods for conservation laws, *Math. Comput.*, *57*, 875–876, doi:10.2307/2938728.

Liang, Y., A. Schiemenz, M. A. Hesse, E. M. Parmentier, and J. S. Hesthaven (2010), High-porosity channels for melt migration in the mantle: Top is the dunite and bottom is the harzburgite and lherzolite, *Geophys. Res. Lett.*, *37*, L15306, doi:10.1029/2010GL044162.

Liang, Y., A. Schiemenz, M. A. Hesse, and E. M. Parmentier (2011), Waves, channels, and the preservation of chemical heterogeneities during melt migration in the mantle, *Geophys. Res. Lett.*, *38*, L20308, doi:10.1029/2011GL049034.

Mazzotti, M., and A. Rajendran (2013), Equilibrium theory-based analysis of nonlinear waves in separation processes, *Annu. Rev. Chem. Biomol. Eng.*, *4*, 119–141, doi:10.1146/annurev-chembioeng-061312-103318.

Navon, O., and E. Stolper (1987), Geochemical consequences of melt percolation: The upper mantle as a chromatographic column, *J. Geol.*, *95*(3), 285–307.

Orr, F. M. (2005), *Theory of Gas Injection Processes*, pp. 1–293, Tie-Line Publications, Holte, Denmark.

Pec, M., B. K. Holtzman, M. Zimmerman, and D. L. Kohlstedt (2015), Reaction infiltration instabilities in experiments on partially molten mantle rocks, *Geology*, *43*(7), 575–578, doi:10.1130/G36611.1.

Pope, G., L. Lake, and F. Helfferich (1978), Cation exchange in chemical flooding: Part 1–Basic theory without dispersion, *Soc. Pet. Eng. J.*, *18*(6), 418–434, doi:10.2118/6771-PA.

Rhee, H. K., R. Aris, and N. Amundson (1970), On the theory of multicomponent chromatography, *Philos. Trans. R. Soc. London A*, *267*, 419–455.

Rhee, H. K., R. Aris, and N. Amundson (1989), *First-Order Partial Differential Equations*, vol. 2, pp. 1–539, Dover Publications, Inc., Mineola, N. Y.

Roozeboom, H. W. B. (1899), Stoechiometrie und Verwandtschaftslehre, *Z. Phys. Chem.*, *28*, 494–517.

Rudge, J. F., D. Bercovici, and M. Spiegelman (2011), Disequilibrium melting of a two phase multicomponent mantle, *Geophys. J. Int.*, *184*(2), 699–718, doi:10.1111/j.1365-246X.2010.04870.x.

Sedqui, A., and B. Guy (2001), Échange chromatographique de deux constituants indépendants entre un fluide aqueux et une solution solide à trois pôles; application à la substitution CaFeMn des grenats de skarn, *C. R. Acad. Sci., Ser. IIA*, *332*(4), 227–234, doi:10.1016/S1251-8050(01)01535-X.

Sobolev, A. V., et al. (2007), The amount of recycled crust in sources of mantle-derived melts, *Science*, *316*(5823), 412–417, doi:10.1126/science. 1138113.

Solano, J. M. S., M. D. Jackson, R. S. J. Sparks, and J. Blundy (2014), Evolution of major and trace element composition during melt migration through crystalline mush: Implications for chemical differentiation in the crust, *Am. J. Sci.*, *314*(5), 895–939, doi:10.2475/05.2014.01.

Spiegelman, M., and P. B. Kelemen (2003), Extreme chemical variability as a consequence of channelized melt transport, *Geochem. Geophys. Geosyst.*, *4*(7), 1055, doi:10.1029/2002GC000336.
Spiegelman, M., P. B. Kelemen, and E. Aharonov (2001), Causes and consequences of flow organization during melt transport: The reaction infiltration instability in compactible media, *J. Geophys. Res.*, *106*, 2061–2077.
Stevenson, D. J. (1989), Spontaneous smallscale melt segregation in partial melts undergoing deformation, *Geophys. Res. Lett.*, *16*, 1067–1070, doi:10.1029/GL016i009p01067.
Szymczak, P., and A. J. C. Ladd (2013), Interacting length scales in the reactive-infiltration instability, *Geophys. Res. Lett.*, *40*, 3036–3041, doi:10.1002/grl.50564.
Valocchi, A. J., R. L. Street, and P. V. Roberts (1981), Transport of ion-exchanging solutes in groundwater: Chromatographic theory and field simulation, *Water Resour. Res.*, *17*, 1517–1527, doi:10.1029/WR017i005p01517.
Venkatraman, A., M. A. Hesse, L. Lake, and R. T. Johns (2014), Analytical solutions for flow in porous media with multicomponent cation exchange reactions, *Water Resour. Res.*, *50*, 5831–5847, doi:10.1002/2013WR015091.
Wachmann, C. (1964), A mathematical theory for the displacement of oil and water by alcohol, *Soc. Pet. Eng. J.*, *4*(03), 250–266.
Walsh, M. P., S. L. Bryant, R. S. Schechter, and L. W. Lake (1984), Precipitation and dissolution of solids attending flow through porous media, *AIChE J.*, *30*(2), 317–328, doi:10.1002/aic.690300222.
Weatherley, S. M., and R. F. Katz (2012), Melting and channelized magmatic flow in chemically heterogeneous, upwelling mantle, *Geochem. Geophys. Geosyst.*, *13*, Q0AC18, doi:10.1029/2011GC003989.
Welge, H., E. E. F. Johnson, S. Ewing Jr., and F. Brinkman (1961), The linear displacement of oil from porous media by enriched gas, *J. Pet. Technol.*, *13*(8), doi:10.2118/1525-G.
White, W. (2013), *Geochemistry*, 660 pp., Wiley-Blackwell.